

Disclosing the properties of low-redshift dual AGN through XMM-Newton and SDSS spectroscopy

Alessandra De Rosa,^{1★} Cristian Vignali,^{2,3} Bernd Husemann,⁴ Stefano Bianchi,⁵ Tamara Bogdanović,⁶ Matteo Guainazzi,⁷ Rubén Herrero-Illana,⁸ S. Komossa,⁹ Emma Kun,¹⁰ Nora Loiseau,¹¹ Zsolt Paragi,¹² Miguel Perez-Torres¹³ and Enrico Piconcelli¹⁴

¹INAF - Istituto di Astrofisica e Planetologia Spaziali (IAPS), via Fosso del Cavaliere, I-133 Roma, Italy

²Dipartimento di Fisica e Astronomia, Alma Mater Studiorum, Università degli Studi di Bologna, Via Gobetti 93/2, I-40129 Bologna, Italy

³INAF - Osservatorio di Astrofisica e Scienza dello Spazio di Bologna, Via Gobetti 93/3, I-40129 Bologna, Italy

⁴Max-Planck Institut für Astronomie, Königstuhl 17, D-69117 Heidelberg, Germany

⁵Dipartimento di Matematica e Fisica, Università degli Studi Roma Tre, via della Vasca Navale 84, I-00146 Roma, Italy

⁶Center for Relativistic Astrophysics, Georgia Institute of Technology, GA 30332 Atlanta, USA

⁷ESA - European Space Research and Technology Centre (ESTEC), Keplerlaan 1, NL-2201AZ Noordwijk, the Netherlands

⁸European Southern Observatory, Alonso de Córdova 3107, Vitacura, Casilla 19001, Santiago de Chile

⁹Max-Planck-Institut für Radioastronomie, Auf dem Hügel 69, D-53121 Bonn, Germany

¹⁰Department of Experimental Physics, University of Szeged, Dóm tér 9, H-6720 Szeged, Hungary

¹¹ESA - European Space Astronomy Centre (ESAC), E-28692 Villanueva de la Cañada, Madrid, Spain

¹²Joint Institute for VLBI ERIC, Postbus 2, NL-7900 AA Dwingeloo, The Netherlands

¹³Centro de Estudios de la Física del Cosmos de Aragón (CEFCA), E-44001 Teruel, Spain

¹⁴INAF - Osservatorio Astronomico di Roma, via Frascati 33, I-00040 Monte Porzio Catone, Italy

Accepted 2018 July 8. Received 2018 June 15; in original form 2018 March 22

ABSTRACT

We report on an optical (SDSS) and X-ray (XMM-Newton) study of an optically selected sample of four dual AGN systems at projected separations of 30–60 kpc. All sources are detected in the X-ray band (0.3–10 keV); seven objects are optically identified as Seyfert, while one source, optically classified as a low-ionization nuclear emission-line region (LINER), is likely powered by accretion in virtue of its relatively high X-ray luminosity (1.2×10^{41} erg s^{-1}). Six of the eight objects are obscured in X-rays with $N_H \geq 10^{23}$ cm^{-2} ; three of these, whose X-ray spectrum is dominated by a reflection component, are likely Compton-thick ($N_H \geq 10^{24}$ cm^{-2}). This finding is in agreement with the hypothesis that galaxy encounters are effective in driving gas inflow toward the nuclear region, thus increasing the obscuration. We compare the absorption properties in our dual AGN with those in larger samples observed in X-rays but selected in different ways (optical, IR, and hard X-rays). We find that the obscured ($N_H \geq 10^{22}$ cm^{-2}) AGN fraction within the larger sample is 84 ± 4 per cent (taking into account the 90 per cent error on the N_H measure) up to large pair separations (~ 100 kpc). This is statistically higher than the fraction of obscured AGN in isolated galaxies found in X-ray surveys.

Key words: galaxies: active – galaxies: interactions – galaxies: nuclei – X-rays: general.

1 INTRODUCTION

Supermassive black holes (SMBHs, with mass 10^6 – 10^9 M_\odot) are ubiquitous in ellipticals and in the bulges of disc galaxies. They are likely to affect the evolution of their host galaxy over cosmological time-scales, as suggested by the tight correlation between black

hole mass and e.g. the bulge stellar velocity dispersion (Ferrarese & Merritt 2000; Gebhardt et al. 2000). The close connection between the formation and evolution of galaxies and of their central SMBHs involves a variety of physical phenomena of great relevance in modern astrophysics (Di Matteo, Springel & Hernquist 2005; Silk & Rees 1998). There is growing evidence that galaxy mergers are the way through which SMBHs can form and evolve, especially at the highest luminosities (Treister et al. 2012). Numer-

* E-mail: alessandra.derosa@iaps.inaf.it

ical simulations have shown that strong inflows in a galaxy merger feed gas to the SMBH, thus powering accretion and triggering the AGN (e.g. Di Matteo et al. 2005). Several observational campaigns in different wavebands have also demonstrated that the fraction of dual AGN¹ is higher in galaxies with a close companion, suggesting that galaxy interaction plays a role in AGN triggering (Ellison et al. 2011; Silverman et al. 2011; Koss et al. 2012; Satyapal et al. 2014; Kocevski et al. 2015). However, other studies found no evidence for an increased AGN fraction in mergers compared to inactive galaxies (e.g. Cisternas et al. 2011; Mechtley et al. 2016).

The detection and characterization of dual AGN at kpc scale is fundamental to understand the BH accretion history. Moreover, dual AGN are the precursor of coalescing binary SMBHs, which are strong emitters of gravitational waves (Abbott et al. 2016).

The search for AGN pairs has received great attention in the last decade (e.g. Bogdanović 2015; Komossa & Zensus 2016), and different methods have been proposed to identify the candidates, depending on their spatial separation. Most of the AGN pairs with 1–100 kpc separations have been identified through extensive optical (Liu et al. 2011; Comerford et al. 2012), radio (Fu et al. 2015; Müller-Sánchez et al. 2015), mid-infrared (mid-IR, Satyapal et al. 2014), and hard X-ray (Koss et al. 2010) surveys. Recent observations have also demonstrated that dual AGN are characterized by enhanced obscuration with respect to isolated AGN in a parent population (Kocevski et al. 2015; Ricci et al. 2017; Satyapal et al. 2017). The high-penetrative power of hard X-rays (above 2 keV) then provides a unique tool in the hunt for multiple active nuclei in a galaxy, because they are less affected by contamination from host galaxy emission and absorption, and are produced in large amounts only by AGN (e.g. Komossa et al. 2003; Guainazzi et al. 2005; Bianchi et al. 2008; Piconcelli et al. 2010; Koss et al. 2011, 2012). The main challenge in this type of study is the need for a statistically significant sample of dual/multiple AGN that covers a wide dynamical range in spatial separations. While a number of AGN pair candidates and merging galaxies have been discovered over the past several years, only a handful of these have eventually been confirmed, usually through intense and observationally expensive multiband follow-up campaigns.

In this paper we characterize four dual AGN systems with separations of 30–60 kpc by means of a multiwavelength study combining X-ray and optical data. We will show that, on the one hand, the optical band is able to select dual AGN candidates even in heavily obscured ($N_H \geq 10^{24} \text{ cm}^{-2}$) systems, on the other hand, X-rays allow to robustly confirm or assess their AGN nature and properly characterize the properties (e.g. column density and intrinsic nuclear emission) of the pair members. Our study aims at contributing to the still poorly explored sample of confirmed dual AGN with tens-of-kpc separation but still below 60 kpc, since their number is relatively limited (about 30 sources, Liu et al. 2011; Koss et al. 2012; Ricci et al. 2017); the present work enlarges that sample with eight new objects, i.e. by about 30 per cent.

The paper is organized as follows: in Section 2 we report on the sample selection, while X-ray observations are introduced in Section 3. The analysis of the optical and X-ray data is carried out in Section 4. The main results are discussed in Section 5 and conclusions are reported in Section 6. Throughout the paper we adopt a concordance cosmology with $H_0 = 70 \text{ km s}^{-1} \text{ Mpc}^{-1}$, $\Omega_\Lambda = 0.7$,

and $\Omega_M = 0.3$. Errors and upper limits quoted in the paper correspond to the 90 per cent confidence level, unless noted otherwise.

2 SAMPLE SELECTION

We draw our dual AGN sample from an optically selected catalogue of AGN pairs (Liu et al. 2011) based on the Sloan Digital Sky Survey (SDSS) Data Release 7 (DR7). We then obtained a ‘master sample’ consisting of 16 systems of Seyfert pairs, 15 with projected separation ranging between 3–60 kpc (2–80 arcsec) and a multiplet (De Rosa et al. 2015), with a redshift distribution $z = 0.03\text{--}0.17$.

The systems with angular separation larger than 10 arcsec have been proposed to be observed with *XMM-Newton*, while closest pairs (angular separation lower than 10 arcsec) will be proposed for *Chandra* observations. Four of the larger separation dual AGN systems are studied in this work (see Table 1); they have projected separations ranging from 30 to 59 kpc. In Fig. 1 we show the SDSS *r*-band image for all our four galaxy pairs and label them in agreement with the nomenclature in Table 1.

3 X-RAY OBSERVATIONS

Both EPIC cameras (pn and MOS) were observing in full-frame mode and with the thin filter applied. Data were reduced using SAS v13.5 with standard settings and the most updated calibration files available at the time of the data reduction. Appropriate filtering to remove periods of high and flaring background was applied; the net exposure for the EPIC cameras is reported in the last column of Table 1.

The EPIC-pn images of the systems are shown in Fig. 2 in two different energy ranges, 0.3–2 keV (left) and 2–8 keV (right). Sources in the *XMM-Newton* fields were detected using the EPIC source detection tool `edetect_chain` in five energy ranges (0.3–0.5 keV, 0.5–1 keV, 1–2 keV, 2–.5 keV, and 4.5–12 keV), adopting a threshold of 3σ . All spectra were extracted from circular regions with radii in the range 11–25 arcsec (see Table 1), depending on the source counts and the separation of the two sources in each system; these regions include $\sim 60\text{--}90$ per cent of the source counts at 1.5 keV in the EPIC cameras. Background spectra were extracted in the same CCD chip using circular regions free from contaminating sources.

Spectra were rebinned in order to have at least 20 counts for each background-subtracted spectral channel and not to oversample the intrinsic energy resolution by a factor larger than 3. In the following we indicate as src1 (src2) the source with the highest (lowest) hard X-ray flux in each pair. Spectral fits for pn and (co-added) MOS cameras were performed in the 0.3–10 keV energy band.

4 DATA ANALYSIS AND RESULTS

4.1 SDSS optical spectra

We retrieved the SDSS DR12 spectra (Alam et al. 2015) for all sources listed in Table 1 from the survey webpage.² All spectra were taken at the location of the galaxies as shown in Fig. 1 and are reported in the Appendix A. We analyse the spectra mainly to infer the narrow emission-line flux for primary diagnostic lines such as $H\beta$, $[O\text{ III}] \lambda 5007$, $[O\text{ I}] \lambda 6300$, $H\alpha$, $[N\text{ II}] \lambda 6583$, and $[S\text{ II}] \lambda \lambda 6717$ and 6730. The analysis of Seyfert 1 and Seyfert 2 galaxy spectra varies significantly so we explain both approaches in the following.

¹In this paper we define dual AGN all galaxy systems containing two AGN with a separation in the range 0.1–100 kpc.

²<http://skyserver.sdss3.org/dr12>

Table 1. Properties of the sources detected in the *XMM-Newton* observations.

Name SDSS (1)	srcID (2)	z (3)	d (arcsec/kpc) (4)	FIRST (mJy) (5)	Date (6)	R_{extr} (arcsec) (7)	pn CR (10^{-3} s^{-1}) (8)	MOS12 CR (10^{-3} s^{-1}) (9)	Net exposure pn/MOS12 (ks) (10)
J094554.41+423840.0	src1	0.0749	21/30	<0.42	2017-Apr-27	15	532 ± 5	116 ± 2	22/52
J094554.49+423818.7	src2	0.0752		1.97 ± 0.14		11	29 ± 1	6.0 ± 0.4	22/52
J103853.28+392151.1	src1	0.0551	40/43	1.19 ± 0.15	2016-May-04	25	254 ± 4	66 ± 1	18/43
J103855.94+392157.5	src2	0.0548		<0.45		20	8.7 ± 0.7	1.5 ± 0.2	18/43
J162640.93+142243.6	src1	0.0482	54/51	1.85 ± 0.14	2016-Aug-26	25	4.2 ± 0.6	1.0 ± 0.2	53/122
J162644.51+142250.7	src2	0.0487		<0.42		25	1.7 ± 0.7	0.5 ± 0.1	53/122
J145627.40+211956.0	src1	0.0446	68/59	<0.45	2017-Jan-12	18	6.0 ± 0.4	0.9 ± 0.1	72/153
J145631.36+212030.1	src2	0.0442		1.87 ± 0.15		18	4.3 ± 0.4	0.7 ± 0.1	72/153

Notes. Col. (1) Name of the source; (2) source ID in each pair (src1 is the one with the highest 2–10 keV flux); (3) redshift from the stellar continuum in obscured AGN and from narrow emission lines in unobscured AGN (see Section 4.1 for details); (4) angular and projected distance between the sources in each system; (5) 1.4 GHz flux densities and 3σ upper limits from the FIRST survey (Becker, White & Helfand 1995); (6) date of the *XMM-Newton* observations; (7) radius of the circular region used to extract the XMM-pn and MOS spectra; (8) and (9) EPIC-pn and combined MOS count rates in the broad-band (0.3–10 keV); (10) EPIC-pn and combined MOS net exposure after filtering correction.

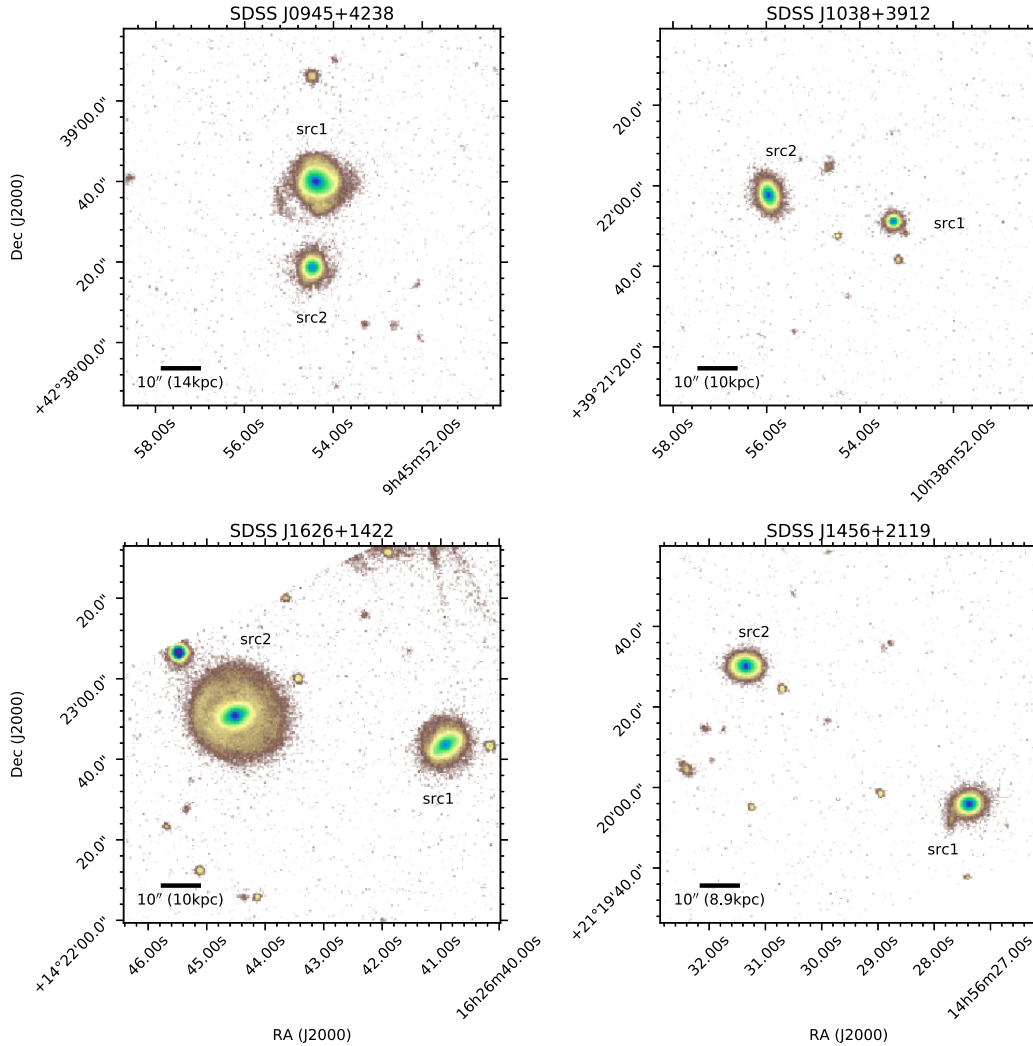


Figure 1. *r*-band SDSS images of our four dual AGN systems shown with a logarithmic surface brightness scaling. The AGN host galaxies are labelled. North is up and East is left. A scale bar indicates 10 arcsec in all panels.

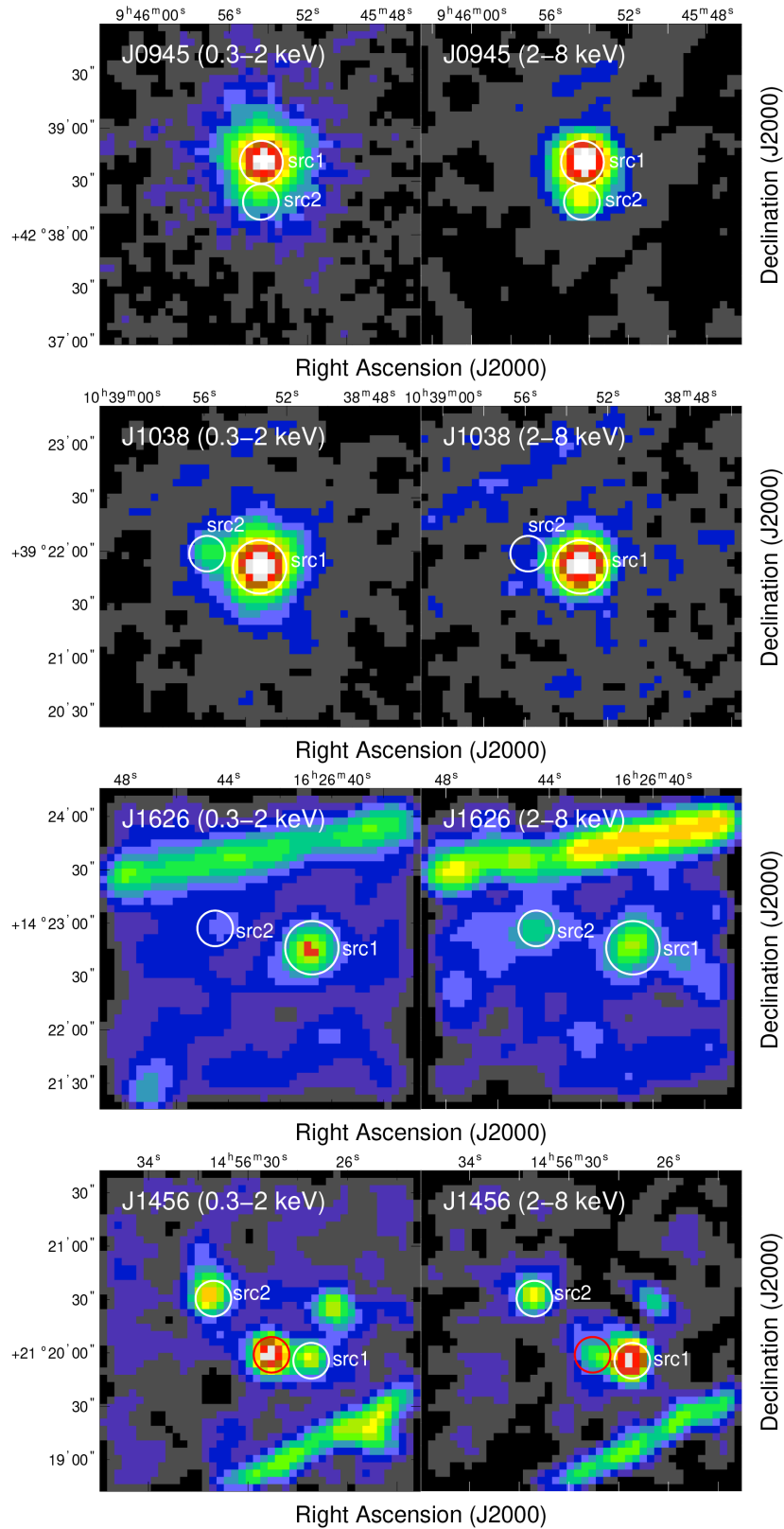


Figure 2. XMM-Newton-pn 3×3 arcmin² region around the systems investigated in this paper. Images in the 0.3–2 keV and 2–8 keV band are shown in the left- and right-hand panels, respectively. From top to bottom: SDSS J0945+4238, SDSS J1038+3921, SDSS J1626+1422, and SDSS J1456+2119. The dual AGN (where src1 is the pair member with the higher 2–10 keV flux) are marked by a solid circle (whose size is not representative of the source extraction region reported in Table 1). North is up and East to the left. Bright elongated regions in J1626 and J1456 images, due to the CCD edges in the pn camera, did not affect our data analysis. The soft X-ray bright excess between src1 and src2 in J1456 field (marked with a red circle) is a background source and is discussed in Section 4.3.

4.1.1 Emission-line modelling of obscured AGN

The light of the nucleus is blocked in obscured AGN. Only the stellar light of the host galaxy and the ionized gas from the narrow-line region (NLR) and/or star forming region can be seen. We measure the emission-line fluxes on top of the stellar continuum light with PYPARADISE software (e.g. Husemann et al. 2016; Weaver et al. 2018). PYPARADISE models the stellar continuum as a superposition of template stellar spectra from the INDO-US stellar library (Valdes et al. 2004) after normalizing both the SDSS and the template spectra with a running mean of 100 pixel, interpolating regions with strong emission lines. A simple Gaussian kernel is used to match the template spectra to the line-of-sight velocity distribution.

The emission-line fluxes are modelled in the residual spectrum after the best fit continuum model is subtracted (see Fig. 3). We couple all Gaussian line profiles in redshift and intrinsic rest-frame velocity dispersion, which reduced the degree-of-freedom and makes the fit robust even for faint emission lines. In some cases a second kinematics component is seen in the [O III] doublet and other forbidden lines which we add as a second system of coupled Gaussians. Errors are obtained using a bootstrap approach, where 100 realizations of the spectrum were generated based on the pixel errors with just 80 per cent of the template spectra and emission-lines are modelled again with the same approach (at fixed stellar kinematics). The resulting emission-line parameters are listed in Table 2 together with one or two velocity dispersions, if required for the respective model. As shown in Fig. 3, we detect a broad component in the [O III] line of SDSS J145631.36+212030.1 with a FWHM of about 1000 km s⁻¹. This indicates a powerful ionized gas outflow in this Compton-thick (CT) AGN.

4.1.2 Emission-line modelling of unobscured AGN

The two unobscured AGN among our dual AGN systems need to be modelled differently as a power-law continuum with broad Balmer lines contribute on top of the stellar continuum and narrow lines. Although the stellar continuum still contributes to the spectrum, we ignore it for our emission-line purposes as we focus here on the broad Balmer line measurements, particularly H α , to estimate the BH mass (e.g. Greene & Ho 2007). First, we subtract a local pseudo-continuum from H β and H α emission-line regions, which we approximate as a linear function based on the emission-line free regions left and right of the H β -[O III] and the H α -[N II] - [S II] regions, respectively. Then, we model the broad Balmer lines with two kinematically independent Gaussians and a set of coupled Gaussians for the narrow emission lines. The coupling of the narrow emission lines is essential for a robust modelling of the [N II] doublet and narrow H α which significantly blend with the broad H α component. Due to the typical blue wing asymmetry in the narrow lines of AGN (e.g. Mullaney et al. 2013), we use two kinematic components coupled for all narrow emission lines. Additionally, strong Fe II emission lines can be present in unobscured AGN spectra which are typically modelled using Fe II template. However, the Fe II template consists only of two Fe II lines in the modelled wavelength region which we model as Gaussians kinematically coupled to the broad H β line components. This way we avoid Fe II template mismatches for our individual targets, but still achieve a very good fit to the spectra (see Fig. 4).

The results for the narrow emission lines are included in Table 2 together with the obscured AGN. The broad-line parameters are listed in Table 3 instead. The broad H α line of SDSS J094554.41+423840.0 is 1442 km s⁻¹ (FWHM). It is significantly

narrower than typical broad-line AGN and therefore is classified as a narrow-line Seyfert 1 (NLSy1). For both AGN we compute the BH masses using the broad H α luminosity and line width based on the calibration of Greene and Ho (2005). This way we avoid that any host galaxy continuum affects our BH mass estimates.

4.2 Emission-line classification

We use the inferred narrow-line fluxes to construct standard emission-line diagnostic diagrams for the unobscured and obscured AGN to classify the emission in star-forming, low-ionization nuclear emission-line region (LINER) like or AGN-like as shown in Fig. 5. Standard demarcation lines are used to separate those ionization sources in the three diagnostics diagrams based on the [O III]/H β , [N II]/H α , [O I]/H α , and [S II]/H α line ratios (Kewley et al. 2001; Kauffmann et al. 2003; Kewley et al. 2006; Cid Fernandes et al. 2010). While such a classification is not necessary for the unobscured AGN as they are already identified as AGN through the presence of broad lines, it is a crucial exercise for the obscured AGN.

We find that all but one of our dual AGN candidates are classified as AGN-like spectra, while one turns out to be a LINER-like spectrum purely based on the emission line ratios. All classifications are consistent in all three diagnostic diagrams which highlight the robustness of the classification in this case. The only exception in our sample is the unobscured AGN SDSS J103853.28+392151.1. While the [N II]/H α line ratio puts the object into the Seyfert-like classification in the classical BPT, the excess in the [O I]/H α and [S II]/H α leads to a LINER-like classification in the other diagrams. This specific excess in the narrow [O I] and [S II] lines with respect to [N II] is very unusual in the AGN population.

The most important point from this analysis is that all dual AGN systems are confirmed as such. Only the ionization source of the LINER-like emission still has to be verified by the X-ray data (described later).

4.3 X-ray spectral analysis

All sources in our sample have been detected at a confidence level $\gtrsim 3\sigma$ in the full X-ray (0.3–10 keV) band. For all sources we fitted the pn and co-added MOS data in the 0.3–10 keV energy band with a baseline model (BLM) composed by (1) an absorbed (zPHABS model in XSPEC with associated cross sections from Balucinska-Church & McCammon 1992) power law that represents the emission of the central regions as due to Comptonization of electrons in a hot-corona by seed photons, probably originated in the accretion disc (the disc-hot corona scenario, see Haardt & Maraschi 1993; Haardt, Maraschi & Ghisellini 1994), (2) a soft, unabsorbed emitting component that reproduces the data at energies lower than ~ 2 keV, the so-called ‘soft excess’. The physical origin of this component is different in obscured and unobscured AGN. In obscured AGN it should be due to star formation activity (Iwasawa et al. 2011), scattering of the primary X-ray emission in Compton-thin circumnuclear gas (Ueda et al. 2007) or a blend of radiative recombination transitions in a photoionized gas (Bianchi, Guainazzi & Chiaberge 2006). In unobscured AGN the soft excess is often attributed to blurred relativistic reflection (Crummy et al. 2006) or Comptonization of the seed optical/UV photons in plasma colder than that responsible for the primary X-ray component; this model is referred to as warm Comptonization (Petrucci et al. 2018, and references therein). To phenomenologically reproduce the soft excess in obscured AGN, we used a scattered power law; the fraction of scattered component

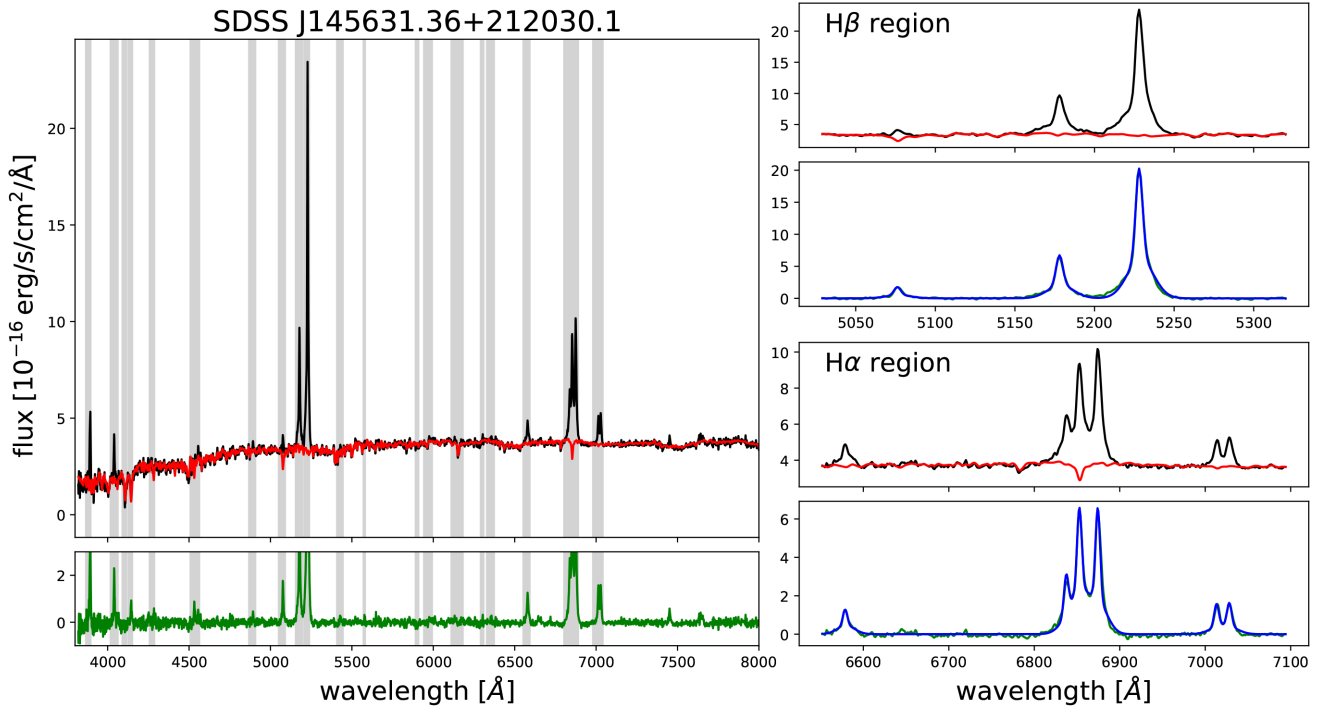


Figure 3. Continuum and emission-line modelling for SDSS J145631.36+212030.1 as an example. *Left-hand panel:* SDSS spectrum is shown as the black line with best fit stellar continuum from PyParadise shown in red. The residual spectrum is shown below in green colour. The grey shaded area highlight regions that were masked during the model because they contain strong emission lines, atmospheric absorption bands, or strong sky-line residuals. *Right-hand panels:* Zoom into the wavelength region focussed around H β (upper spectra) and H α (lower spectra). Again the data is shown in black and the stellar continuum model in red. Below the best fit emission-line model is shown in blue on top of the green residual spectrum. Two Gaussian components are clearly needed to provide a good model to the emission lines in this case.

Table 2. Optical emission lines parameters from the SDSS spectra for the narrow line components.

SrcID	H β	[O III] λ 5007	[O I] λ 6300 Flux [10^{-16} erg cm s $^{-1}$]	H α	[N II] λ 6583	[S II] λ 6717,30	σ_{narrow} [km s $^{-1}$]	σ_{broad} [km s $^{-1}$]	Class
SDSS J0945+4238									
src1	14.3 ± 2.4	70.2 ± 3.2	3.7 ± 1.0	61.4 ± 6.7	32.7 ± 5.2	19.1 ± 1.6	101 ± 9	243 ± 13	AGN1
src2	47.4 ± 0.1	201.8 ± 0.1	14.2 ± 0.2	236.4 ± 0.1	165.2 ± 0.1	89.3 ± 0.4	143 ± 1	...	AGN2
SDSS J1038+3921									
src1	8.2 ± 1.0	47.8 ± 1.0	18.5 ± 0.7	32.7 ± 2.0	32.7 ± 1.4	33.5 ± 1.0	160 ± 3	...	AGN1
src2	12.2 ± 0.1	125.7 ± 0.1	6.1 ± 0.2	47.1 ± 0.1	32.7 ± 0.1	24.6 ± 0.5	101 ± 1	...	AGN2
SDSS J1626+1422									
src1	16.5 ± 0.3	179.1 ± 0.6	17.4 ± 0.8	73.8 ± 0.7	72.8 ± 0.6	45.6 ± 1.4	83 ± 1	289 ± 3	AGN2
src2	2.9 ± 0.2	3.8 ± 0.1	1.1 ± 0.2	7.1 ± 0.3	10.2 ± 0.3	6.6 ± 0.6	129 ± 10	...	LINER
SDSS J1456+2119									
src1	5.3 ± 0.6	40.1 ± 1.6	2.7 ± 0.5	21.5 ± 1.4	13.3 ± 0.9	7.8 ± 1.3	75 ± 2	184 ± 7	AGN2
src2	16.5 ± 0.6	203.0 ± 0.5	16.9 ± 0.6	80.9 ± 1.5	72.6 ± 1.6	32.5 ± 1.2	97 ± 1	450 ± 2	AGN2

is measured by the parameter f_{scatt} , which is the ratio between the luminosity of the scattered component versus the primary component in 0.3–2 keV energy range. For unobscured AGN, we reproduced the soft excess with a phenomenological model, a thermal blackbody emission. For sources with low X-ray photon statistics, the primary power-law photon index has been frozen to $\Gamma = 1.9$, as expected for AGN (e.g. Bianchi et al. 2009). The power-law and the blackbody components are not physical models, but they are able to reproduce the excess through the softer energies, including any

possible contribution from the star formation to the luminosity in the ≈ 0.3 –2 keV band; a more detailed discussion about the estimate of the star formation rate (SFR) is presented in Section 5.

When statistically needed, we included in the fit physically motivated components to fit narrow-band features as emission or absorption lines. Reprocessing from circumnuclear material, the Compton hump, was taken into account assuming a semi-infinite optically-thick slab (pexrav model in xSPEC, Magdziarz & Zdziarski 1995). The inclination and the metallicity of the slab were fixed to 45° and

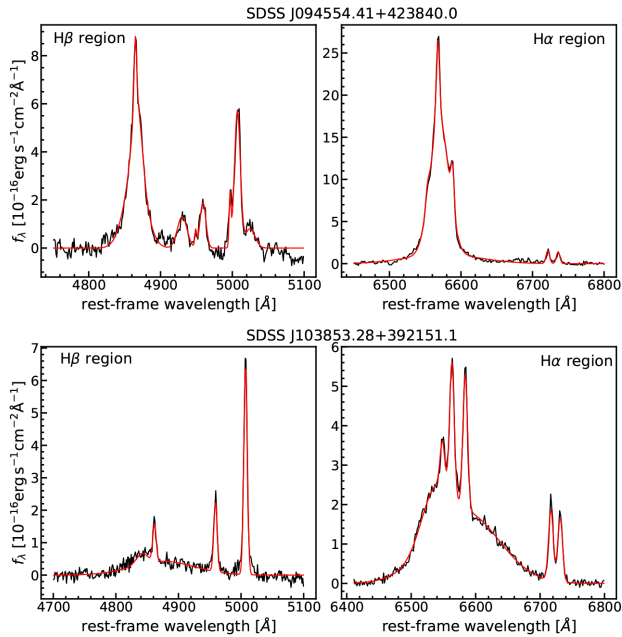


Figure 4. Emission line modelling of the two unobscured type 1 AGN spectra. J0945 is shown in the upper panels with strong FeII doublet while J1038 is shown in the bottom panels. The continuum is approximated by a local linear relation and the broad H β and H α lines are independently fitted by two or three broad Gaussian components. The narrow lines are coupled in intrinsic redshift and velocity dispersion for one or two systems of Gaussians.

to solar, respectively. The reflection fraction was measured using the parameter $R = \Omega/2\pi$, where Ω is the covering factor of the reflecting material. The whole model is absorbed by Galactic gas with column density obtained by Dickey and Lockman (1990).³

The luminosity of the [O III] λ 5007 emission line is considered a good indicator of the intrinsic luminosity of the AGN, in both type 1 and type 2 (see also Section 4.1), once extinction within the NLR and, at some level its geometry, are properly taken into account. In particular, we use the Balmer decrement (H α /H β ratio) to correct the [O III] emission for the extinction. To derive the $L_{[\text{O III}]}$ corrected for extinction, we used the relation from Bassani et al. (1999) which assumes the Cardelli, Clayton, and Mathis (1989) extinction law and an intrinsic Balmer decrement equal to three; this value represents the case for the NLR (Osterbrock & Ferland 2006). The ratio between the X-ray luminosity and the $L_{[\text{O III}]}$ λ 5007 has been therefore used as an indirect measurement of N_{H} . The $L_{\text{x}}/L_{[\text{O III}]}$ ratio has been investigated by several authors using different samples of type 1 and type 2 AGN (Mulchaey et al. 1994; Bassani et al. 1999; Heckman et al. 2005; Lamastra et al. 2009; Vignali et al. 2010). In particular, Marinucci et al. (2012) measured $\log(L_{\text{x}}/L_{[\text{O III}]}) = -0.76$ (0.1 dex dispersion) in a sample of CT AGN, while for Compton-thin AGN Lamastra et al. (2009) found $\log(L_{\text{x}}/L_{[\text{O III}]}) = 1.09$ (0.63 dex dispersion). These values are useful to shed further light on the source classification based on the X-ray spectral analysis.

In the following, we report the X-ray properties of each dual system and compare them with the classification obtained from the analysis of the optical spectra. In Fig. 6, we plot the pn+MOS12 best fit spectra (upper panels) and residuals (lower panels) for all four systems. Best fit values for all systems are reported in Table 4.

4.3.1 SDSS J0945+4238

The sources in J0945+4238 are detected with a S/N ratio of 100 (src1) and 25 (src2) in the 0.3–10 keV band. The soft (0.3–2 keV) and hard (2–8 keV) band images (see Fig. 2, upper left panels) are suggestive of the presence of heavy obscuration in src2. Given the relative proximity between the two sources (21 arcsec), we estimated that the PSF wings of src1 contaminates src2 in the hard band by ≤ 20 per cent.

When fitted with the BLM model, src1 does not require any absorption component ($N_{\text{H}} \leq 3 \times 10^{20} \text{ cm}^{-2}$, see Table 4) in addition to the Galactic one, and the X-ray spectrum looks like a type 1 Seyfert, in agreement with the optical classification (see Table 2). The residuals with respect to a power-law model plus a thermal component still show an excess in the hardest X-ray band and in the Fe line region around 6 keV. The fit marginally improves ($\Delta\chi^2 = 5$) by adding a cold reflection component (pexrav model in XSPEC); the best fit of the reflection fraction is $R = 2.2 \pm 1.8$. The fit further improves by adding two narrow emission lines, whose best fit energies are 2.81 ± 0.03 keV and 3.91 ± 0.07 keV, with equivalent width of $\text{EW} = 80 \pm 30$ eV and 110 ± 50 eV, respectively. These lines, clearly visible in both pn and MOS12 data, are statistically significant (the F-test probability is 99.7 per cent for both lines). Furthermore, we note that these features lie in an energy range where no calibration issues should be present (i.e. the effective area of pn and MOS cameras is smooth). The closest transitions at these energies are Si XV or Si XVI (2.45 keV and 2.62 keV) and Ca XVIII or Ca XIX (3.9 and 4.1 keV), nevertheless we cannot provide a physically convincing explanation for their presence of both lines in the J0945+4238 src1 spectrum. On the basis of the available optical imaging data, it seems unpalatable that these emission lines come from other sources in the X-ray source extraction region of src1.

The X-ray spectrum of src2 is typical of a type 2 AGN, as expected by the optical diagnostics (see Fig. 5), with an X-ray obscured primary continuum and a soft component. Fitting src2 with the BLM provides good results: the primary continuum is obscured by a column density of $N_{\text{H}} = 24_{-6}^{+8} \times 10^{22} \text{ cm}^{-2}$. The soft power law contributes more than 10 per cent to the emission below 2 keV ($f_{\text{scatt}} \sim 10$). However, this value must be considered just an upper limit due to the possible contamination of src1.

The system SDSS J0945+4238 therefore comprises a NLSy1, X-ray unobscured AGN, and a type 2 Compton-thin AGN.

4.3.2 SDSS J1038+3921

The nuclei in J1038+3921 are detected in 0.3–10 keV energy band with an S/N of 68 and 13, respectively (see Fig. 2, upper right panels).

When fitting src1 data with the BLM model we only find an upper limit to the absorption component ($N_{\text{H}} \leq 3 \times 10^{20} \text{ cm}^{-2}$), and the X-ray spectrum is consistent with expectations in case of a type 1 Seyfert galaxy. This is also in agreement with the optical classification (see Table 2). A narrow Fe K α line is marginally (2σ) required by the fit; its rest-frame energy is $6.6_{-0.3}^{+0.2}$ keV and the equivalent width is $\text{EW} = 130_{-10}^{+150}$ eV. Including a cold reflection component provides a negligible improvement ($\Delta\chi^2 = 2$) in the spectral fit, with the best fit reflection fraction $R = 2.0_{-1.5}^{+2.0}$, and the photon index being still consistent with the previous value within errors.

Fitting src2 with the BLM, we obtain a very flat primary photon index above 2 keV, $\Gamma \sim -1$, and a measured 2–10 keV luminos-

³<http://heasarc.gsfc.nasa.gov/cgi-bin/Tools/w3nh/w3nh.pl>

Table 3. Broad H α measurements for the two unobscured AGN.

Object	$f_{\text{H}\alpha}$ [10^{-14} erg s $^{-1}$ cm $^{-2}$]	$\log(L_{\text{H}\alpha})$ [erg s $^{-1}$]	FWHM $_{\text{H}\alpha}$ [km s $^{-1}$]	$\log(M_{\text{BH}})$ [M_{\odot}]
SDSS 0945 + 4238	7.06 ± 0.38	41.99 ± 0.02	1442 ± 75	6.6 ± 0.1
SDSS 1038 + 3921	3.24 ± 0.17	41.37 ± 0.02	5557 ± 375	7.5 ± 0.1

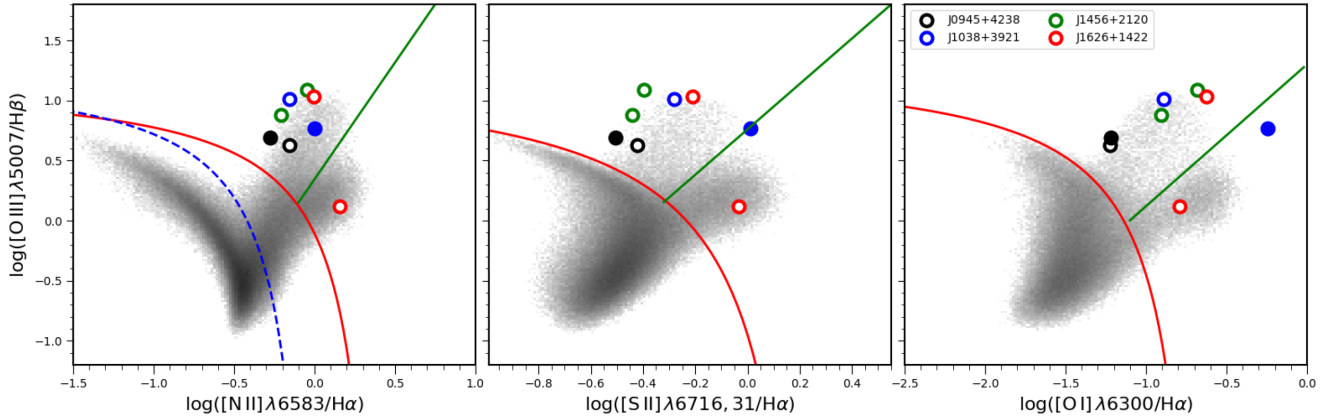


Figure 5. Classical emission-line ratio diagnostic diagrams for all spectra of our dual AGN systems. Errors bars for these high signal-to-noise ratio (S/N) spectra are smaller than the symbol size. Obscured AGN are denoted by open circles and unobscured AGN are marked as filled circles. The distribution of line ratios in the overall galaxy population are shown as the grey density map taken from the SDSS DR7 MPA-JHU value-added catalog (Brinchmann et al. 2004). Red solid line marks the maximum line starburst as inferred by Kewley et al. 2001, the blue dashed line represents the empirical SFG boundary proposed by Kauffmann et al. 2003, and the green solid line is the empirically proposed division between AGN and LINERs (Kewley et al. 2006; Cid Fernandes et al. 2010).

ity of $\sim 3 \times 10^{40}$ erg s $^{-1}$. The Balmer decrement ($\text{H}\alpha/\text{H}\beta \sim 3.9$) leads to a de-reddened [O III] luminosity of about 2×10^{41} erg s $^{-1}$ (see Table 2) which, in turn, gives an X-ray to optical luminosity ratio of $\log(L_x/L_{[\text{O III}]}) = -0.9$. As described above, this low value is strongly indicative of a heavily obscured, possibly CT AGN (e.g. Lamastra et al. 2009; Vignali et al. 2010). We test then the possibility that the direct X-ray radiation is totally absorbed by a CT medium ($N_{\text{H}} \geq 10^{24}$ cm $^{-2}$) and that we are observing is the reflected component in the *XMM-Newton* observing band. To this goal, we replace the absorbed hard X-ray primary continuum with a pure reflection spectrum (`perxav` in `xSPEC`), as expected in case of a CT AGN, and leave a soft X-ray scattered component dominating at low energies. This model typically provides a good representation of the X-ray spectra of highly obscured AGN, at the level of statistical quality of the objects discussed in this paper (e.g. Lanzuisi et al. 2015). The fit obtained using this model is good: the observed luminosity is $\sim 10^{41}$ erg s $^{-1}$ and no significant residuals are visible (see Fig. 6). Assuming the intrinsic X-ray luminosity to be 80 times the observed L_x (Lamastra et al. 2009; Marinucci et al. 2012), we obtained $L_x = 8 \times 10^{42}$ erg s $^{-1}$ and $\log(L_x/L_{[\text{O III}]}) = 1$, in a very good agreement with the values found in type 2 Seyfert galaxies once the observed luminosities are corrected for the obscuration. The observed spectrum below 4 keV is completely dominated by the soft power-law component. However, when considering the estimated intrinsic luminosity, the scattered component f_{scatt} contributes about 1 per cent to the 0.5–2 keV luminosity, but this should be considered as a lower limit, due to the fact that the primary continuum below 10 keV is completely obscured from the CT gas.

Summarizing, the system SDSS J1038+3921 consists of an optical type 1, X-ray unobscured AGN, and one CT AGN optically associated with a type 2 AGN.

4.3.3 SDSS J1626+1422

Both sources in the SDSS J1626+1422 system are detected in the broad-band with a signal-to-noise ratio of 15 and 10 (see Fig. 2, bottom left panels), respectively. For what concerns src1, the low signal-to-noise ratio of the data does not allow us to constrain the primary photon index, which we fixed to the typical value found in Seyfert galaxies ($\Gamma = 1.9$, e.g. Bianchi et al. 2009). When the BLM is applied to its EPIC spectra, src1 appears highly obscured, with N_{H} in the range $\sim (20\text{--}220) \times 10^{22}$ cm $^{-2}$. Correcting the observed X-ray luminosity for the obscuration (best fit value of $N_{\text{H}} = 67 \times 10^{22}$ cm $^{-2}$) we obtain $8 (6) \times 10^{41}$ erg s $^{-1}$ in the 2–10 (0.5–2) keV band, with the soft component contributing ~ 3 per cent to the 0.5–2 keV unabsorbed luminosity. As in the case of SDSS J1038+3921 (src2), we fit the data replacing the transmission model with a pure reflection model in the 2–10 keV band, while the soft X-ray data still modelled with a power law. The fit is still good ($\chi^2/\text{dof} = 38/39$) and the observed 2–10 keV luminosity is about 10^{41} erg s $^{-1}$, which translates into an intrinsic luminosity of 8×10^{42} erg s $^{-1}$ by adopting the factor 80 (valid for heavily obscured sources) as described above. In this case the soft X-ray component would contribute to ~ 3 per cent (f_{scatt}) of the total unabsorbed luminosity in the 0.5–2 keV band. We cannot statistically distinguish among the two scenarios (Compton-thick versus Compton-thin), however, the solid conclusion is that the *XMM-Newton* spectrum of src1 is consistent with a highly obscured, possibly CT AGN.

We fit src2 *XMM-Newton* data with the BLM model; given the low quality of the spectrum, we tied the soft photon index to the primary and fixed their value to 1.9 as a measure in a larger sample of LINER galaxies (González-Martín et al. 2009). Although we only have an upper limit for src2 in the soft band (below 2 keV), the hard X-ray data allowed us to reproduce the shape of the continuum and measure the absorption column density. The source is absorbed by

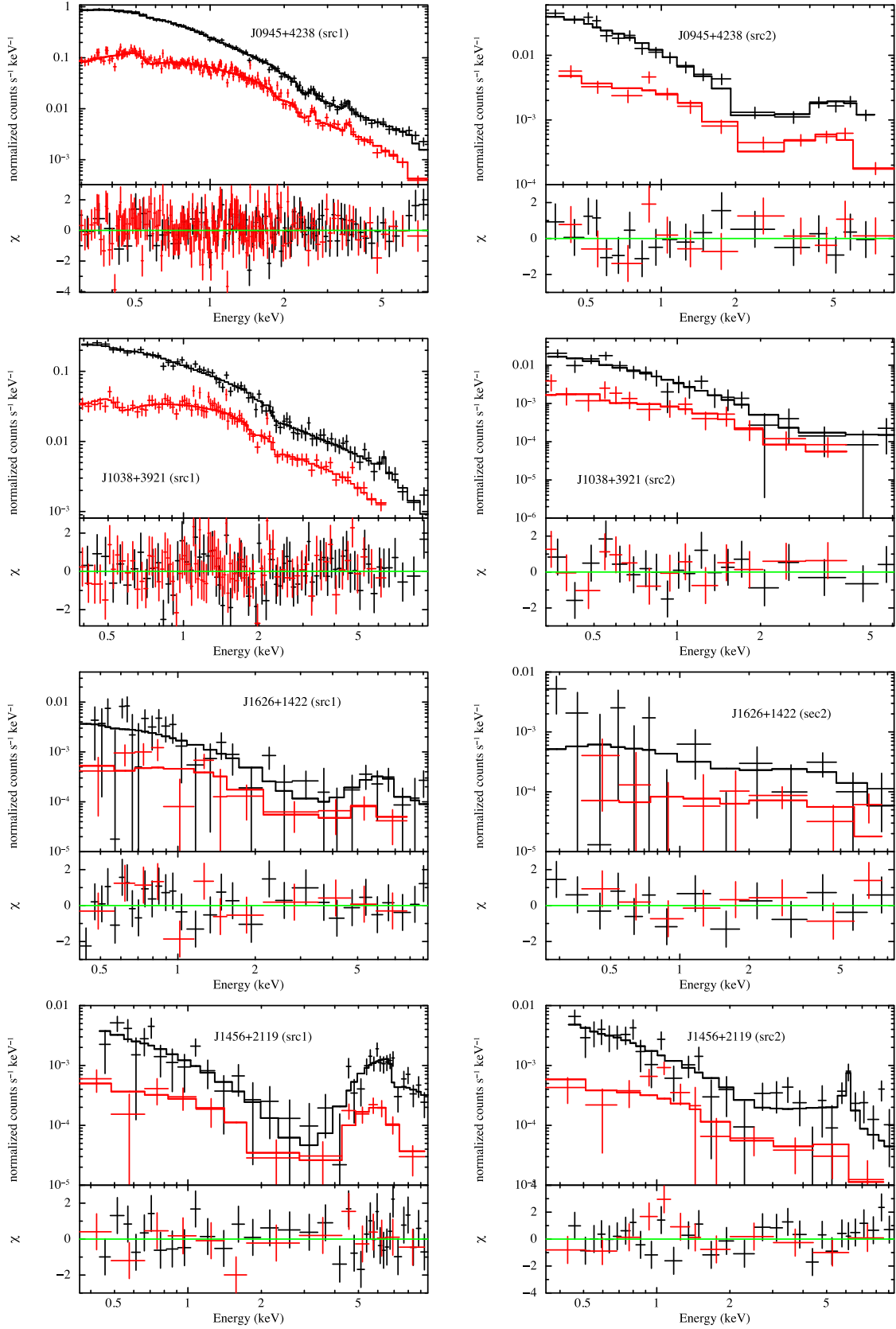


Figure 6. XMM-Newton spectra of the eight sources. From top to bottom: SDSS J0945+4238, SDSS J1038+3921, SDSS J1626+1422, and SDSS J1456+2119. Spectral data and best fit models are reported in the top panels (EPIC-pn: black; MOS12: red), while data-to-model residuals (in units of σ) are shown in the lower panels.

Table 4. XMM-Newton spectral analysis results.

SrcID (1)	Γ (2)	Γ_{soft}/kT (3)	N_{H} (4)	f_{scatt} (5)	$F_{\text{soft}}^{\text{oss}}$ (6)	$F_{\text{hard}}^{\text{oss}}$ (7)	$L_{\text{x}}^{\text{oss}}$ (8)	L_{x} (9)	L_{Bol} (10)	$L_{[\text{O III}]}$ (11)	χ^2/dof (12)	X-ray class (13)
SDSS J0945+4238												
src1	$2.4^{+0.1}_{-0.1}$	0.11 ± 0.01	<0.03	-	68 ± 1	50 ± 3	7.0 ± 0.3	7.0 ± 0.3	112	0.2	224/231	U
src2	1.9^*	2.6 ± 0.2	24^{+8}_{-6}	13 ± 5	3.5 ± 0.2	19 ± 2	2.4 ± 0.3	6.9 ± 0.3	110	1.1	22/26	C-thin
SDSS J1038+3921												
src1	1.62 ± 0.07	$0.12^{+0.03}_{-0.03}$	<0.03	-	27 ± 1	55 ± 5	4.2 ± 0.2	4.2 ± 0.2	53	0.08	140/152	U
src2	1.9^*	3.0 ± 0.3	>100	>1	1.0 ± 0.1	1.6 ± 1.0	0.2 ± 0.1	8^{\dagger}	132	0.2	21/29	C-thick
SDSS J1626+1422												
src1	1.9^*	2.2 ± 0.5	67^{+150}_{-50}	3 ± 2	0.4 ± 0.1	$2.3^{+0.8}_{-2.0}$	0.2 ± 0.1	$0.8^{+0.3}_{-0.7}$	8	0.3	36/39	C-thick $\dagger\dagger$
src2	1.9^*	$=\Gamma$	6^{+12}_{-4}	<1	<0.2	1.2 ± 0.8	0.5 ± 0.1	0.12 ± 0.08	1	0.001	13/18	C-thin
SDSS J1456+2119												
src1	1.9 ± 0.9	2.8 ± 0.5	75^{+28}_{-23}	0.7 ± 0.4	$0.28^{+0.04}_{-0.02}$	$8.6^{+0.5}_{-3.1}$	$0.4^{+0.1}_{-0.1}$	$3.7^{+0.2}_{-1.3}$	50	0.04	43/45	C-thin
src2	1.9^*	2.8 ± 0.5	>100	3 ± 2	0.40 ± 0.05	2.3 ± 0.5	0.2 ± 0.1	8^{\dagger}	132	0.3	45/37	C-thick

Notes. (1) Source ID in each pair; (2) Primary photon index; (3) Soft X-ray photon index of the scattered power law (obscured AGN - C-thin/thick) or temperature of the thermal blackbody component (unobscured AGN - U); (4) Absorption column density in units of 10^{22} cm^{-2} ; (5) Scattered fraction (%), for the type 2 AGN, obtained as the ratio between the luminosity of the scattered component and the primary continuum in 0.3–2 keV range (see Section 4); (6) Observed soft (0.5–2 keV) and (7) hard (2–10 keV) flux in units of $10^{-14} \text{ erg cm}^{-2} \text{ s}^{-1}$; (8) Observed, and (9) absorption-corrected, rest-frame 2–10 keV luminosity in units of $10^{42} \text{ erg s}^{-1}$. \dagger For CT sources, the intrinsic 2–10 keV luminosity has been obtained by multiplying the observed luminosity by 80 (Lamastra et al. 2009; Marinucci et al. 2012); (10) Bolometric luminosity in units of $10^{42} \text{ erg s}^{-1}$ obtained using Marconi et al. (2004) bolometric corrections; (11) De-reddened [O III] luminosity in units of $10^{42} \text{ erg s}^{-1}$ (see Table 2); (12) χ^2 over degrees of freedom of the best fit model (see Section 4); (13) Classification from the X-ray spectral analysis presented in this work (U: unobscured; C-thin: Compton-thin; C-thick: CT). *: Fixed parameter during the fit. $\dagger\dagger$ CT candidate.

cold gas, with $N_{\text{H}} \sim 6 \times 10^{22} \text{ cm}^{-2}$; the derived intrinsic, rest-frame 2–10 keV luminosity is $1.2 \times 10^{41} \text{ erg s}^{-1}$, and $\log(L_{\text{x}}/L_{[\text{O III}]}) = 1.5$ is within the range expected for an AGN obscured by Compton-thin gas. Optical diagnostic diagrams suggest this source to be a LINER; however, the derived X-ray luminosity, at face value, is above the mean value found in the systematic X-ray study of the largest sample of LINERs thus far carried out (González-Martín et al. 2009). In their investigation, González-Martín et al. (2009) have shown that when LINERs contain an AGN, their average 2–10 keV luminosity is $\log L_{\text{x}} = 40.22 \pm 1.24$, higher than in cases when the powering source is not clearly associated with an active nucleus ($\log L_{\text{x}} = 39.33 \pm 1.16$).

Summarizing, SDSS J1626+1422 system comprises one CT AGN candidate (optically classified as a type 2 AGN) and an X-ray obscured LINER, likely accretion-driven on the basis of the relatively high X-ray luminosity.

4.3.4 SDSS J1456+2119

The dual AGN in the SDSS J1456+2119 system are detected with a signal-to-noise ratio of 20 and 18 (see Fig. 2, bottom right panels), respectively. Fitting src1 with the BLM provides a good fit: the source is highly obscured, with $N_{\text{H}} = 75^{+28}_{-23} \times 10^{22} \text{ cm}^{-2}$. The spectrum below 2 keV is reproduced using a soft unabsorbed power law with steep photon index ($\Gamma_{\text{soft}} \sim 2.6$). The contribution of this component to the 0.5–2 keV intrinsic luminosity is $f_{\text{scatt}} \sim 0.7$ per cent. It is worth noting that a third X-ray source is visible close to src1 (~ 23 arcsec separation); we extracted and analysed the X-ray spectrum of this source. Due to the XMM-Newton EPIC PSF (~ 90 per cent of the encircled energy fraction at 1.5 keV lies in a circular region

of 30 arcsec radius), this source only marginally (<25 per cent) contaminates the 0.5–2 keV spectrum of src1.

Fitting src2 with the BLM provides an unphysically hard photon index ($\Gamma = -1$) and an X-ray luminosity of $\sim 10^{41} \text{ erg s}^{-1}$. The presence of heavy obscuration is confirmed by the X-ray versus de-reddened [O III], (see Table 2) luminosity ratio, $\log(L_{\text{x}}/L_{[\text{O III}]}) = -0.5$. Fitting the XMM-Newton data with a reflection-dominated model, we obtain a good fit and no systematic residuals are observed (see Fig. 6). The observed 2–10 keV luminosity of $10^{41} \text{ erg s}^{-1}$ would translate into an intrinsic luminosity of $8 \times 10^{42} \text{ erg s}^{-1}$ (using the factor 80 discussed previously), and a $\log(L_{\text{x}}/L_{[\text{O III}]}) = 1.3$. A narrow Fe K α line is marginally (3σ) required by the fit. Its rest-frame energy is $6.3^{+0.2}_{-0.1} \text{ keV}$ and its EW = $0.98^{+0.86}_{-0.43} \text{ keV}$ is consistent with the expectations in case of heavily obscured objects. The soft X-ray spectrum is well modelled with a steep power law, whose contribution to the 0.5–2 keV intrinsic luminosity is $f_{\text{scatt}} \sim 3$ per cent.

XMM-Newton data of system SDSS J1456+2119 are therefore consistent with a pairs of obscured AGN, one in the Compton-thin and one in the Compton-thick regime.

5 DISCUSSION

In this work we characterized the X-ray properties of an optically selected sample of dual AGN systems, drawn from SDSS (Liu et al. 2011) and classified using standard emission-line ratio diagnostics (Baldwin, Phillips & Terlevich 1981). With the main goal of characterizing their multiwavelength properties, we started an observational campaign of a well-defined sample of dual AGN with projected separation below 60 kpc. In this paper we reported on the study of four systems at kpc-scale separation observed with

SDSS and XMM-Newton. Because Liu et al. (2011) used a standard automatic procedure to classify sources in their SDSS sample, we carefully re-analysed the optical spectra, and the results of our fitting procedure are reported in Section 4.

5.1 The emission properties of dual AGN sample

Through X-ray data we confirm the presence of two AGN in all analysed systems, and the X-ray classification is in perfect agreement with the optical classification, as predicted by the AGN unification scenarios (Antonucci 1993) X-ray unabsorbed AGN are associated with broad-line AGN (BL AGN), and X-ray obscured sources with narrow-line AGN (NL AGN) in the optical band. The X-ray spectra are reproduced with an absorbed primary power law and a second unabsorbed component in the soft X-ray band (< 2 keV) to reproduce the soft excess. Additional spectral components to model the reprocessing of the nuclear radiation (e.g. Fe emission line and Compton reflection) are also introduced to model the two type 1 Seyfert (J1038-src1 and J0945-src1). The range of bolometric luminosity in our sample is $\log(L_{\text{bol}}/\text{erg s}^{-1}) \sim 42\text{--}44.1$, and the average value of the primary photon index and intrinsic X-ray luminosity (in the 2–10 keV band) measured in our sample is 1.91 (when left free to vary in the fit, with 0.19 standard deviation) and 3.7×10^{42} erg s $^{-1}$ (0.19 standard deviation), respectively. These values are in a very good agreement with those measured in larger samples of AGN in isolated systems (Bianchi et al. 2009; De Rosa et al. 2012).

The soft component (soft excess) in the type 2 AGN is reproduced with a scattered power law and contributes about $f_{\text{scatt}} \sim 0.5\text{--}10$ per cent to the total intrinsic luminosity in the 0.5–2 keV band in our sample. This value is in good agreement with the fraction of soft X-ray emission component commonly observed in type 2 AGN, and is likely due to the emission from the NLR (Bianchi et al. 2006). However, it could be also produced through Thomson scattering of the primary X-ray emission in photoionized gas (Ueda et al. 2007). Finally, soft X-ray emission could also be due to star-forming regions from a population of X-ray binaries (Ranalli, Comastri & Setti 2003). Low-photon statistics in the soft band does not allow to disentangle individual contributions from star formation and photoionized gas. To estimate the emission coming from star formation activity, we used the radio flux density at 1.4 GHz from the FIRST survey (see Table 1) as an indicator for SFR (Condon 1992). In four over eight sources we obtained an upper limit for the SFR, while for four sources an estimate of the SFR was derived. Then we used the SFR versus L_x relation of Ranalli et al. (2003) to evaluate the contribution of the SFR to the X-ray luminosity. The contribution of the SFR to the X-ray emission ranges from 1 to 10 per cent in our obscured sources, then we conclude that the SFR has a limited effect on the X-ray luminosity.

The origin of the soft excess in type 1 AGN is still unclear and commonly interpreted as due to relativistic reflection from the innermost region in the accretion disc (Crummey et al. 2006) or the effect of thermal Comptonization of the disc photons in a warm, optically thick corona (Magdziarz et al. 1998; Petrucci et al. 2018). We reproduced the soft excess in the unabsorbed AGN with a simple phenomenological model, i.e. thermal component (a blackbody). Although the blackbody is not a physical representation of the spectral feature, it is able to reproduce the soft excess with respect to the power law in both the two type 1 AGN. We found a temperature $kT \sim 0.1$ keV for both type 1 AGN (J0945-src1 and J1038-src1); these are typical values found in Seyfert 1s (Gierliński & Done 2004). The fraction of the soft X-ray component with respect to the

primary emission in the 0.5–2 keV band for the two type 1 AGN is ~ 30 and ~ 70 per cent, respectively. From our optical analysis (see Table 2) we classified J0945+4238 src1 as a NLSy1, which is expected to have a larger soft X-ray component with respect to broad-line AGN, possibly due to a higher accretion rate and lower BH mass (Boller, Brandt & Fink 1996; Jin et al. 2012). We used $H\alpha$ luminosity and FWHM (see Table 3) in order to compute the BH mass for the NLSy1 J0945-src1 obtaining $4 \times 10^6 M_{\odot}$ and, in turn, an Eddington luminosity of 5×10^{44} erg s $^{-1}$ and an Eddington ratio $\lambda_{\text{Edd}} \sim 0.23$ (assuming the bolometric correction given by Marconi et al. 2004, see Table 4). This value is higher with respect to average values of λ_{Edd} measured in large sample of BL AGN in the same luminosity bin (mean $\lambda_{\text{Edd}} = 0.033$ with 0.38 dispersion, see e.g. Lusso et al. 2012). The Eddington ratio of J1038+3921 src1, $\lambda_{\text{Edd}} \sim 0.01$ (see Table 3), is perfectly consistent with larger sample of BL AGN. The spectral index of the primary power law in J0945+4238 src1 is significantly higher than the other sources, 2.4 versus 1.9, as also observed in X-ray spectra of NLSy1 (and references therein, Jin et al. 2012).

5.2 The nature of obscuration

Six out of the eight sources (75 per cent of the sample) show evidence for high obscuration by cold gas (column density $N_{\text{H}} \gtrsim 10^{23}$ cm $^{-2}$). The number of AGN with $N_{\text{H}} \gtrsim 10^{24}$ cm $^{-2}$ is in the range 2–4 when 90 per cent confidence errors on the column density are considered (see Table 4). Although our sample is definitely too small to make any strong conclusion in terms of statistical incidence of obscured AGN in dual systems, we note that the fraction of CT AGN in our sample of dual AGN is 25–50 per cent, i.e. higher than the fraction of hard X-ray selected CT AGN in isolated systems in a similar luminosity interval (BAT: 27 ± 4 per cent, Ricci et al. 2015, *NuSTAR*: ~ 4 per cent, Marchesi et al. 2018). Recently, it has been suggested (Ricci et al. 2017) that AGN in multiple systems in a late stage of merging (with a projected distance $d \leq 10$ kpc) are often type 2 AGN due to the huge amount of gas and dust obscuration channelled towards the nuclear region by the close galaxy encounter. Furthermore, in a sample of 44 UltraLuminous IR Galaxies (ULIRG) from the GOALS survey (Sanders et al. 2003) in the local universe, it has been demonstrated that the fraction of CT AGN in late mergers is higher (65_{-13}^{+12} per cent) than in local isolated hard X-ray selected AGN (27_{-4}^{+4} per cent, Ricci et al. 2017), while it is marginally higher than isolated AGN in early mergers (35_{-12}^{+13} per cent). The increasing of the obscuration with the disturbed or interacting morphology of the galaxy host has been also observed up to higher redshift (up to $z = 1.5$) using X-ray *Chandra* data from deep surveys (Kocevski et al. 2015). These authors have analysed 154 heavily obscured AGN and compared their morphologies with control samples composed of moderately obscured and unobscured AGN. They found that the fraction of galaxies undergoing mergers is higher in AGN with N_{H} above 3×10^{23} cm $^{-2}$ with respect to unobscured AGN with $N_{\text{H}} < 10^{22}$ cm $^{-2}$ ($7.8_{-1.3}^{+1.9}$ versus $21.5_{-3.3}^{+4.2}$ per cent). X-rays (Kocevski et al. 2015; Ricci et al. 2017) as well as more recent mid-IR colour selection (Satyapal et al. 2017) strongly suggest that AGN in late state of merging (< 10 kpc) are highly absorbed (but see also Ellison et al. 2017), with N_{H} above 10^{24} cm $^{-2}$. All these observational results suggest that CT AGN in dual systems correspond to a phase where the supermassive black hole is still accreting gas during an early stage of an interaction or merging.

The systems investigated here have projected separations larger than 10 kpc, in the range 30–60 kpc, so they might be pre-existing AGN–AGN pairs, not triggered by encounters. They are likely to un-

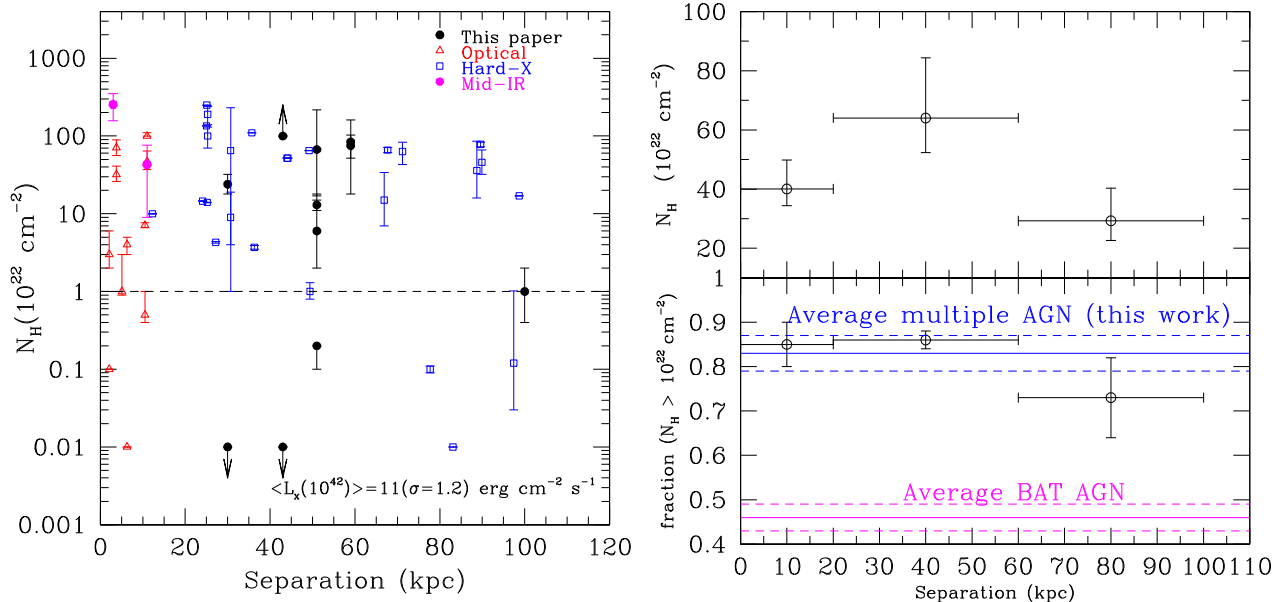


Figure 7. *Left.* Absorbing column density N_{H} versus projected separation between the nuclei for known multiple systems from this work and literature. In particular, we used the systems investigated in this work and in De Rosa et al. (2015; black circles); from literature: (1) optically selected in SDSS (Guainazzi et al. 2005; Bianchi et al. 2008; Piconcelli et al. 2010; Liu et al. 2013; red triangles); (2) hard X-ray selected mainly with *Swift*/BAT (Koss et al. 2012; blue squares); (3) IR selected from GOALS (Ricci et al. 2017; magenta circles). *Right.* Upper panel represents the values of the absorption column density of the samples reported in the left diagram, averaged in three ranges of projected galaxies separations: 0–20, 20–60, and 60–100 kpc. Lower panel: Fraction of AGN in dual/multiple systems with N_{H} above 10^{22} cm^{-2} as a function of the projected separation. Blue lines represent the average value as obtained for the large sample investigated in this paper (61 sources, see left-hand panels) when 90 per cent errors on N_{H} are taken into account. Magenta lines represent the *Swift*/BAT average values and 1σ error as reported in Ricci et al. (2015) in the same bin of 2–10 keV luminosity.

undertake a pre- or early-merging phase, where galaxies are separated (i.e. prior to the first encounter) and not yet strongly interacting. In this respect we also note that the system J0945+4238, containing the AGN pair at the closest separation (30 kpc, see Table 1), shows some evidence of interaction on galaxy scale with the possible presence of an initial tidal bridge (see Fig. 1, first panel on the left).

The small number of systems investigated here does not allow any strong statistical argument, therefore we decided to analyse additional sources selected in different wavebands and for which a measure of the absorption column density can be derived from X-ray observations. In Fig. 7 (left-hand panel) we plot the absorption column density of AGN sources hosted in a dual/multiple system as a function of the projected separation for the sample presented here and for additional systems observed in X-rays and taken from literature. We included the following dual AGN systems: (i) optically selected from the SDSS (Guainazzi et al. 2005; Bianchi et al. 2008; Piconcelli et al. 2010; Liu et al. 2013; De Rosa et al. 2015); (ii) hard X-ray selected as obtained by the *Swift*-BAT survey (Koss et al. 2012); (iii) mid-infrared selected as obtained by GOALS (Sanders et al. 2003; Ricci et al. 2017). The total sample comprises of 61 AGN with 2–10 keV average luminosity $(11 \pm 2) \times 10^{42} \text{ erg s}^{-1}$ (standard deviation $\sigma = 1.2 \times 10^{42} \text{ erg s}^{-1}$) and average $N_{\text{H}} = (50_{-9}^{+15}) \times 10^{22} \text{ cm}^{-2}$ (standard deviation $\sigma = 4 \times 10^{22} \text{ cm}^{-2}$). In the right (upper) panel of Fig. 7, we show the column density N_{H} in three different bins of projected separation, and in the lower panel the fraction of sources showing obscuring column density $N_{\text{H}} > 10^{22} \text{ cm}^{-2}$.

Although the available measurements of dual systems hosting AGN are sparse, it seems plausible that obscuration (N_{H} above 10^{22} cm^{-2}) is a common property also during the early stage of merging.

The fraction of AGN hosted in dual or multiple systems, up to large separation, with absorption larger than 10^{22} cm^{-2} is 84 ± 4 per cent (see blue lines in the right-bottom panel of Fig. 7, accounting for the 90 per cent error on the N_{H} measurement). The fraction of isolated AGN that show absorption above 10^{22} cm^{-2} as observed by BAT (Ricci et al. 2015) is 46 ± 3 per cent (magenta lines in Fig. 7, right-bottom panel). This comparison suggests that the ‘environment’ of dual AGN systems is different, namely more obscuring than that of isolated AGN. We do not find evidence for a trend of increasing N_{H} with decreasing separation (see the right-upper panel in Fig. 7).

Blecha et al. (2017) presented numerical simulations of AGN in galaxy mergers, showing an increase of N_{H} as the distance decreases. This effect is due to merger dynamics; the median value of N_{H} was about $3 \times 10^{23} \text{ cm}^{-2}$, in good agreement with the value we have found in the large sample of dual systems investigated here (see Fig. 7). However, their simulations only probe absorption on relatively large scales (above ~ 50 pc, then absorption from the torus on pc-scale is not considered), therefore the N_{H} value should be considered as a lower limit.

Although heavy absorption can prevent the detections of dual AGN (up to large-scale separation) through X-ray surveys (Koss et al. 2012), our study demonstrates that a multiband approach provides a successful strategy to detect and characterize dual AGN in late- and early-stage of merging.

In this scenario the type 1 unobscured Seyfert detected in J0945-src1 and J1038-src1 are unusual, especially considering their projected separation of few tens of kpc. Unobscured AGN have recently been detected with *Chandra* in a dual system at close separation (~ 8 kpc, Ellison et al. 2017). Studies of larger samples of X-ray selected AGN in galaxy pairs indicate a non-negligible fraction of X-ray unobscured AGN (Guainazzi et al., in preparation). It is intriguing

to speculate that X-ray unobscured members of AGN pairs may represent systems, where the efficiency of funnelling gas and dust towards the nuclear region is low, or where the nuclear environment has been cleared up by powerful AGN outflows. Our spectroscopic analysis unveiled a powerful outflow in a heavily obscured AGN (J1456+2119), that could constitute a step in a sequence of events, of which unobscured members of AGN pairs represent the terminal stage.

Selecting AGN by their mid-infrared colours and emission-line properties, Juneau et al. (2013) investigated the star-forming activity and morphology of obscured AGN. Galaxy mergers are expected to fuel AGN as well as intense episodes of star formation, with the AGN deeply obscured in a large amount of gas. In their analysis they found that the obscured AGN fraction is higher among galaxies with elevated SF rates, possibly due to galaxy interactions. This result is consistent with an evolutionary scenario in which the abundant gas supply in the obscured AGN phase enhances the star formation. The SF rate and the obscuration both decline as the fuel decreases (Alexander & Hickox 2012; Ellison et al. 2016). However, a similar study is not possible in our four dual AGN systems because of the lack of far-IR data, needed to properly estimate the star formation rates in their host galaxies.

6 SUMMARY AND CONCLUSIONS

In this work we have presented the optical and X-ray study on four dual AGN at kpc-scale separation. They belong to a large sample of multiple AGN systems selected from SDSS (Liu et al. 2011) and classified using standard emission-line ratio diagnostics. As a first step, our observational campaign characterizes the properties of a well-defined sample of dual AGN with projected separation in the range 30–60 kpc using SDSS and XMM-Newton. In this paper we have focused on the X-ray absorption properties of the sample and how they compare to larger samples of dual AGN at various scale separations and to isolated systems. Our main results are summarized below.

(i) Through standard optical emission-line ratio diagnostics (see Fig. 5) all objects are identified as AGN except one that is a LINER; due to its relatively high X-ray luminosity, the LINER emission is likely accretion driven.

(ii) All sources are detected in X-rays, either in the soft and/or high-energy band. The X-ray and optical classification perfectly matches each other: X-ray unabsorbed AGN are associated with broad-line AGN, and X-ray obscured sources with narrow-line AGN in the optical band. The X-ray spectral properties of all systems (L_x and Γ , when left free to vary in the fit) are in agreement with values found in large samples of isolated local AGN (see Table 4).

(iii) Six over eight objects are obscured by cold gas ($\log N_H > 23$), and the fraction of CT AGN ($\log N_H > 24$) is 25–50 per cent (accounting for the 90 per cent error on the N_H measure). This fraction is higher than that found in isolated hard X-ray selected AGN (BAT: 27 ± 4 per cent, Ricci et al. 2015; *NuSTAR*: ~ 4 per cent, Marchesi et al. 2018).

(iv) In order to statistically probe systems at different separations, we compared the absorption properties in our pairs with those in larger samples observed in X-rays and selected in different ways (optical, IR, and hard X-rays, see Fig. 7), for a total of 61 sources. We find that the fraction of obscured ($N_H \geq 10^{22} \text{ cm}^{-2}$) AGN is 84 ± 4 per cent up to large-scale separations ($\sim 100 \text{ kpc}$), i.e. higher with respect to isolated AGN as observed by BAT (46 ± 3 per cent, Ricci et al. 2015).

(v) In this scenario, two systems presented here manifest a different behaviour, being composed of an unobscured type 1 AGN and an obscured (CT in one case) AGN. Although the number statistics is still too small, we can speculate that X-ray unobscured AGN in pairs may represent systems characterized by a low efficiency of funnelling gas and dust towards the nuclear region, or where the nuclear environment has been cleared up by powerful AGN outflows.

Although the sample we presented in this work is limited due to the paucity of measurements of dual/multiple AGN, our analysis is in agreement with the hypothesis that galaxy encounters are effective in driving gas inflow, thus increasing the obscuration (Kocevski et al. 2015; Ricci et al. 2017). In addition, our findings suggest that the environment of dual AGN systems is different – more obscured – with respect to isolated AGN up to wide separations ($\sim 100 \text{ kpc}$). We can speculate that these systems with larger amounts of obscuring gas have a high efficiency of funnelling gas and dust towards the nuclear region. Heavy absorption can prevent the X-ray detections of dual AGN and it has been proposed to explain the disagreement between optical and X-ray fraction of mergers (Koss et al. 2012). Our analysis shows instead that the combined optical and X-ray observing strategy represents a powerful tool to select and confirm dual AGN systems, even if heavily obscured, in interacting galaxies. A multiband approach, as the one proposed in the MAGNA project,⁴ is a successful strategy in order to detect and characterize dual AGN in late- and early-stage of merging. Recently, we have obtained deep JVLA dual-band radio and LBT data for the master sample galaxy pairs described in Section 2 (in particular, LBT data for the systems at closer separation, below 10 arcsec). These data are being analysed with the aim of characterizing their radio morphology and spectral behaviour, and will be presented in forthcoming papers (Herrero-Illana et al., in preparation; Husemann et al., in preparation).

ACKNOWLEDGEMENTS

The authors would like to thank the referee for her/his constructive comments and suggestions. The authors, members of the MAGNA project (<http://www.issibern.ch/teams/agnactivity/Home.html>), gratefully acknowledge support of the International Space Science Institute (ISSI), Bern, Switzerland, and the hospitality of the Lorentz Center for international workshops, where one portion of this work was carried out. The Italian authors acknowledge financial contribution from the agreement ASI-INAF n.2017-14-H.O. CV acknowledges financial support from the Italian Space Agency under the contract ASI-INAF I/037/12/0. We thank the hospitality of ESA-ESTEC where part of this work has been carried out, BH is grateful for financial support from the ESA-ESTEC visitor program.

Funding for SDSS-III has been provided by the Alfred P. Sloan Foundation, the Participating Institutions, the National Science Foundation, and the U.S. Department of Energy Office of Science. The SDSS-III web site is <http://www.sdss3.org/>. SDSS-III is managed by the Astrophysical Research Consortium for the Participating Institutions of the SDSS-III Collaboration including the University of Arizona, the Brazilian Participation Group, Brookhaven National Laboratory, Carnegie Mellon University, University of Florida, the French Participation Group, the German Participation Group, Harvard University, the Instituto de Astrofísica de Canarias,

⁴<http://www.issibern.ch/teams/agnactivity/Home.html>

the Michigan State/Notre Dame/JINA Participation Group, Johns Hopkins University, Lawrence Berkeley National Laboratory, Max Planck Institute for Astrophysics, Max Planck Institute for Extraterrestrial Physics, New Mexico State University, New York University, Ohio State University, Pennsylvania State University, University of Portsmouth, Princeton University, the Spanish Participation Group, University of Tokyo, University of Utah, Vanderbilt University, University of Virginia, University of Washington, and Yale University.

REFERENCES

- Abbott B. P. et al., 2016, *Phys. Rev. Lett.*, 116, 061102
- Alam S. et al., 2015, *ApJS*, 219, 12
- Alexander D. M., Hickox R. C., 2012, *New Astron. Rev.*, 56, 93
- Antonucci R., 1993, *ARA&A*, 31, 473
- Baldwin J. A., Phillips M. M., Terlevich R., 1981, *PASP*, 93, 5
- Balucinska-Church M., McCammon D., 1992, *ApJ*, 400, 699
- Bassani L., Dadina M., Maiolino R., Salvati M., Risaliti G., Della Ceca R., Matt G., Zamorani G., 1999, *ApJS*, 121, 473
- Becker R. H., White R. L., Helfand D. J., 1995, *ApJ*, 450, 559
- Bianchi S., Guainazzi M., Chiaberge M., 2006, *A&A*, 448, 499
- Bianchi S., Chiaberge M., Piconcelli E., Guainazzi M., Matt G., 2008, *MNRAS*, 386, 105
- Bianchi S., Guainazzi M., Matt G., Fonseca Bonilla N., Ponti G., 2009, *A&A*, 495, 421
- Blecha L., Snyder G. F., Satyapal S., Ellison S. L., 2017, *MNRAS*, 478, 3056
- Bogdanović T., 2015, in Sopuerta C. F., ed., *Proc. Astrophysics and Space Science*, Vol. 40, Gravitational Wave Astrophysics. Springer-Verlag, Switzerland, p. 103
- Boller T., Brandt W. N., Fink H., 1996, *A&A*, 305, 53
- Brinchmann J., Charlot S., White S. D. M., Tremonti C., Kauffmann G., Heckman T., Brinkmann J., 2004, *MNRAS*, 351, 1151
- Cardelli J. A., Clayton G. C., Mathis J. S., 1989, *ApJ*, 345, 245
- Cid Fernandes R., Stasińska G., Schlickmann M. S., Mateus A., Vale Asari N., Schoenell W., Sodré L., 2010, *MNRAS*, 403, 1036
- Cisternas M. et al., 2011, *ApJ*, 726, 57
- Comerford J. M., Gerke B. F., Stern D., Cooper M. C., Weiner B. J., Newman J. A., Madsen K., Barrows R. S., 2012, *ApJ*, 753, 42
- Condon J. J., 1992, *ARA&A*, 30, 575
- Crummy J., Fabian A. C., Gallo L., Ross R. R., 2006, *MNRAS*, 365, 1067
- De Rosa A. et al., 2012, *MNRAS*, 420, 2087
- De Rosa A. et al., 2015, *MNRAS*, 453, 214
- Di Matteo T., Springel V., Hernquist L., 2005, *Nature*, 433, 604
- Dickey J. M., Lockman F. J., 1990, *ARA&A*, 28, 215
- Ellison S. L., Patton D. R., Mendel J. T., Scudder J. M., 2011, *MNRAS*, 418, 2043
- Ellison S. L., Teimoorinia H., Rosario D. J., Mendel J. T., 2016, *MNRAS*, 458, L34
- Ellison S. L., Secrest N. J., Mendel J. T., Satyapal S., Simard L., 2017, *MNRAS*, 470, L49
- Ferrarese L., Merritt D., 2000, *ApJ*, 539, L9
- Fu H., Myers A. D., Djorgovski S. G., Yan L., Wrobel J. M., Stockton A., 2015, *ApJ*, 799, 72
- Gebhardt K. et al., 2000, *ApJ*, 539, L13
- Gierliński M., Done C., 2004, *MNRAS*, 349, L7
- González-Martín O., Masegosa J., Márquez I., Guainazzi M., Jiménez-Bailón E., 2009, *A&A*, 506, 1107
- Greene J. E., Ho L. C., 2005, *ApJ*, 630, 122
- Greene J. E., Ho L. C., 2007, *ApJ*, 667, 131
- Guainazzi M., Piconcelli E., Jiménez-Bailón E., Matt G., 2005, *A&A*, 429, L9
- Haardt F., Maraschi L., 1993, *ApJ*, 413, 507
- Haardt F., Maraschi L., Ghisellini G., 1994, *ApJ*, 432, L95
- Heckman T. M., Ptak A., Hornschemeier A., Kauffmann G., 2005, *ApJ*, 634, 161
- Husemann B., Bennert V. N., Scharwächter J., Woo J.-H., Choudhury O. S., 2016, *MNRAS*, 455, 1905
- Iwasawa K. et al., 2011, *A&A*, 529, A106
- Jin C., Ward M., Done C., Gelbord J., 2012, *MNRAS*, 420, 1825
- Juneau S. et al., 2013, *ApJ*, 764, 176
- Kauffmann G. et al., 2003, *MNRAS*, 346, 1055
- Kewley L. J., Dopita M. A., Sutherland R. S., Heisler C. A., Trevena J., 2001, *ApJ*, 556, 121
- Kewley L. J., Groves B., Kauffmann G., Heckman T., 2006, *MNRAS*, 372, 961
- Kocevski D. D. et al., 2015, *ApJ*, 814, 104
- Komossa S., Zensus J. A., 2016, in Meiron Y., Li S., Liu F.-K., Spurzem R., eds, *Proc. IAU Symp. 312, Star Clusters and Black Holes in Galaxies across Cosmic Time*. Kluwer, Dordrecht, p. 13
- Komossa S., Burwitz V., Hasinger G., Predehl P., Kaastra J. S., Ikebe Y., 2003, *ApJ*, 582, L15
- Koss M. et al., 2011, *ApJ*, 735, L42
- Koss M., Mushotzky R., Veilleux S., Winter L., 2010, *ApJ*, 716, L125
- Koss M., Mushotzky R., Treister E., Veilleux S., Vasudevan R., Trippe M., 2012, *ApJ*, 746, L22
- Lamastra A., Bianchi S., Matt G., Perola G. C., Barcons X., Carrera F. J., 2009, *A&A*, 504, 73
- Lanzuisi G. et al., 2015, *A&A*, 578, A120
- Liu X., Shen Y., Strauss M. A., Hao L., 2011, *ApJ*, 737, 101
- Liu X., Civano F., Shen Y., Green P., Greene J. E., Strauss M. A., 2013, *ApJ*, 762, 110
- Lusso E. et al., 2012, *MNRAS*, 425, 623
- Magdziarz P., Zdziarski A. A., 1995, *MNRAS*, 273, 837
- Magdziarz P., Blaes O. M., Zdziarski A. A., Johnson W. N., Smith D. A., 1998, *MNRAS*, 301, 179
- Marchesi S., Ajello M., Marcotulli L., Comastri A., Lanzuisi G., Vignali C., 2018, *ApJ*, 854, 49
- Marconi A., Risaliti G., Gilli R., Hunt L. K., Maiolino R., Salvati M., 2004, *MNRAS*, 351, 169
- Marinucci A., Bianchi S., Nicastro F., Matt G., Goulding A. D., 2012, *ApJ*, 748, 130
- Mechtley M. et al., 2016, *ApJ*, 830, 156
- Mulchaey J. S., Koratkar A., Ward M. J., Wilson A. S., Whittle M., Antonucci R. R. J., Kinney A. L., Hurt T., 1994, *ApJ*, 436, 586
- Mullaney J. R., Alexander D. M., Fine S., Goulding A. D., Harrison C. M., Hickox R. C., 2013, *MNRAS*, 433, 622
- Müller-Sánchez F., Comerford J. M., Nevin R., Barrows R. S., Cooper M. C., Greene J. E., 2015, *ApJ*, 813, 103
- Osterbrock D. E., Ferland G. J., 2006, in Osterbrock D. E., Sausalito G. J. F., eds, *Astrophysics of Gaseous Nebulae and Active Galactic Nuclei*. Univ. Science Books, California
- Petrucci P.-O., Ursini F., De Rosa A., Bianchi S., Cappi M., Matt G., Dadina M., Malzac J., 2018, *A&A*, 611, A59
- Piconcelli E. et al., 2010, *ApJ*, 722, L147
- Ranalli P., Comastri A., Setti G., 2003, *A&A*, 399, 39
- Ricci C. et al., 2017, *MNRAS*, 468, 1273
- Ricci C., Ueda Y., Koss M. J., Trakhtenbrot B., Bauer F. E., Gandhi P., 2015, *ApJ*, 815, L13
- Sanders D. B., Mazzarella J. M., Kim D.-C., Surace J. A., Soifer B. T., 2003, *AJ*, 126, 1607
- Satyapal S. et al., 2017, *ApJ*, 848, 126
- Satyapal S., Ellison S. L., McAlpine W., Hickox R. C., Patton D. R., Mendel J. T., 2014, *MNRAS*, 441, 1297
- Silk J., Rees M. J., 1998, *A&A*, 331, L1
- Silverman J. D. et al., 2011, *ApJ*, 743, 2
- Treister E., Schawinski K., Urry C. M., Simmons B. D., 2012, *ApJ*, 758, L39
- Ueda Y. et al., 2007, *ApJ*, 664, L79
- Valdes F., Gupta R., Rose J. A., Singh H. P., Bell D. J., 2004, *ApJS*, 152, 251
- Vignali C., Alexander D. M., Gilli R., Pozzi F., 2010, *MNRAS*, 404, 48
- Weaver J. R. et al., 2018, *A&A*, 614, 14

APPENDIX A: FIGURES OF THE OPTICAL SPECTRAL MODELLING

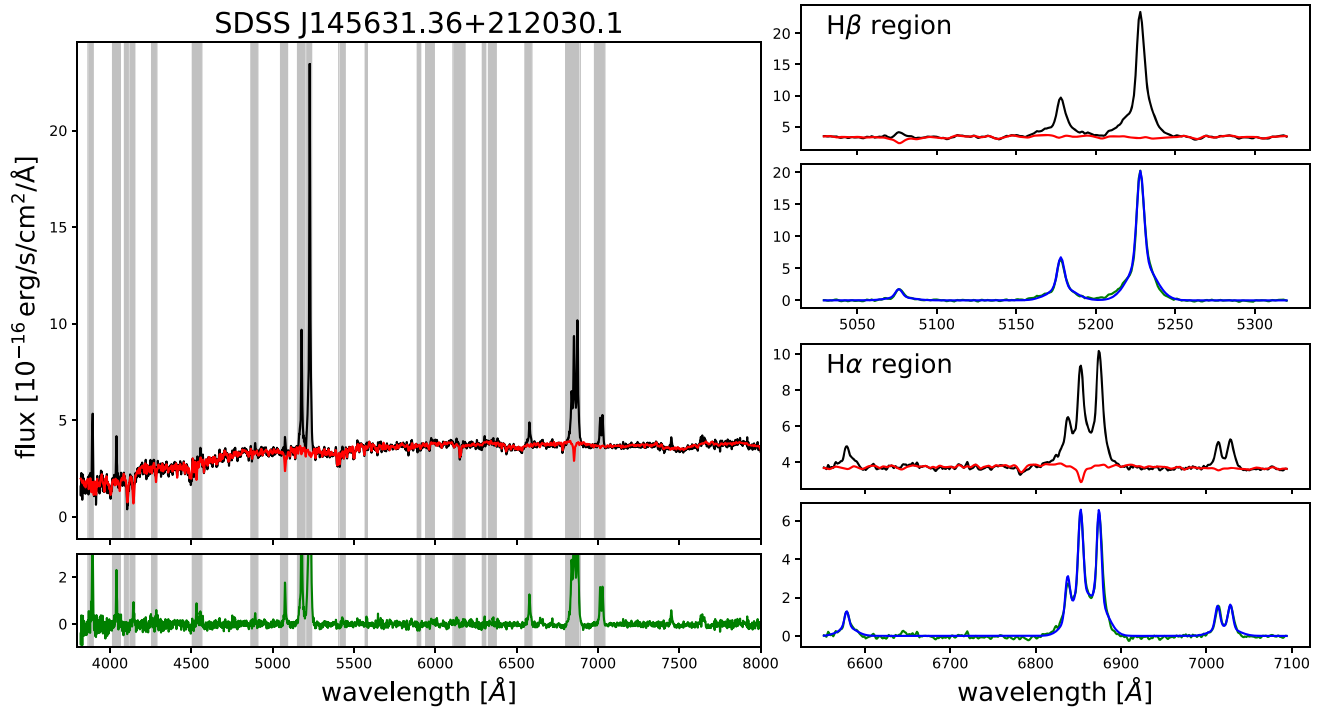


Figure A1. Same as Fig. 3 for SDSS J145631.36+212030.1.

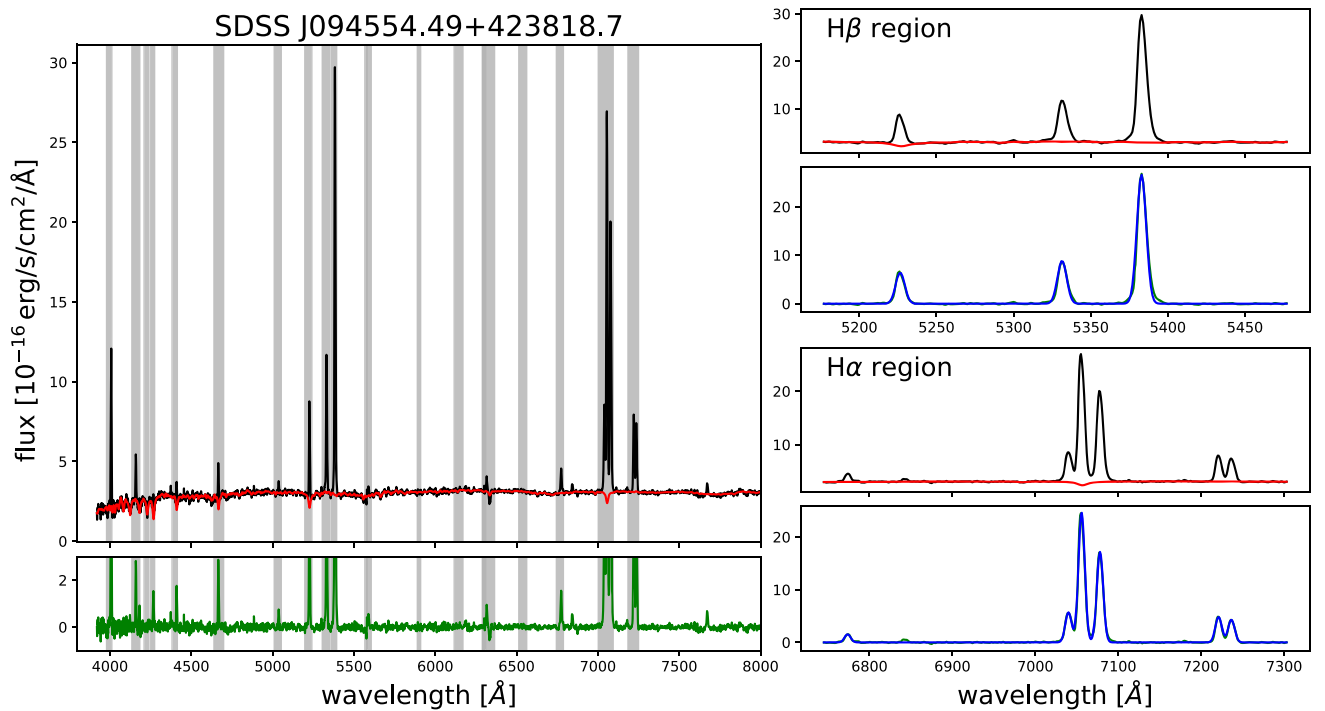


Figure A2. Same as Fig. 3 for SDSS J094554.49+423818.7.

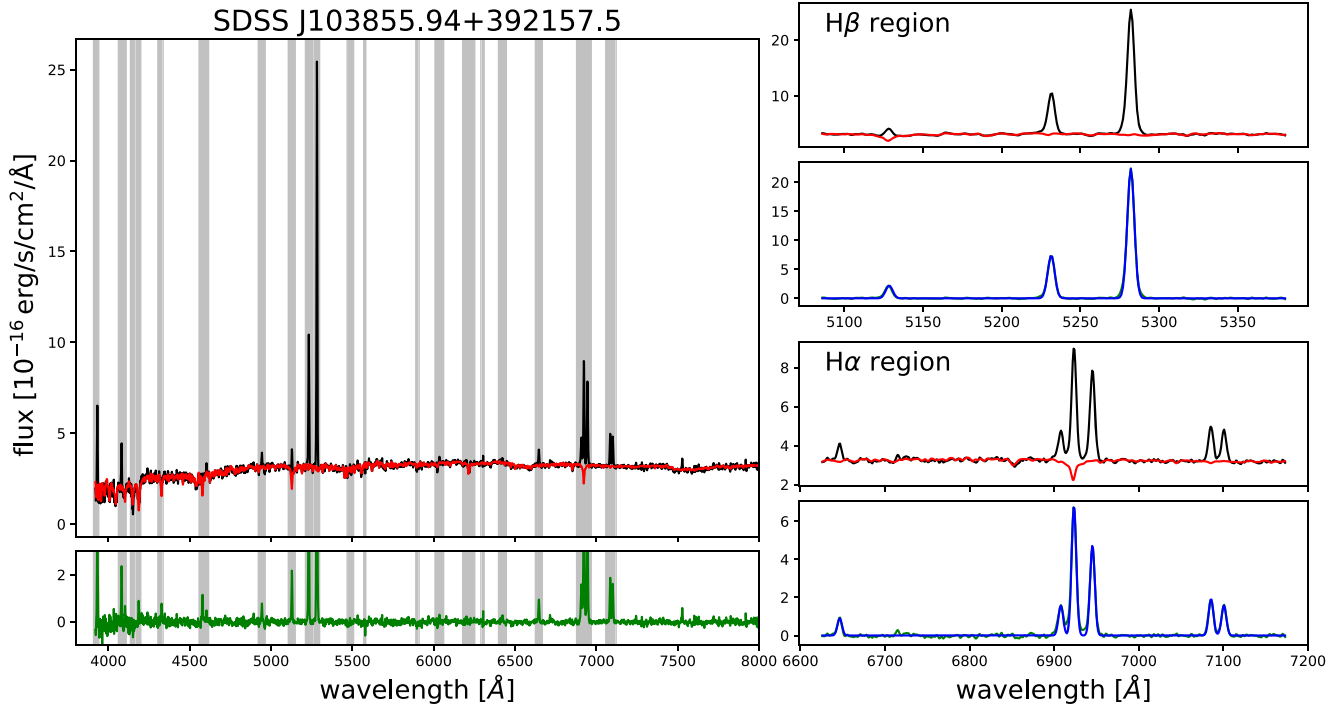


Figure A3. Same as Fig. 3 for SDSS J103855.94+392157.5.

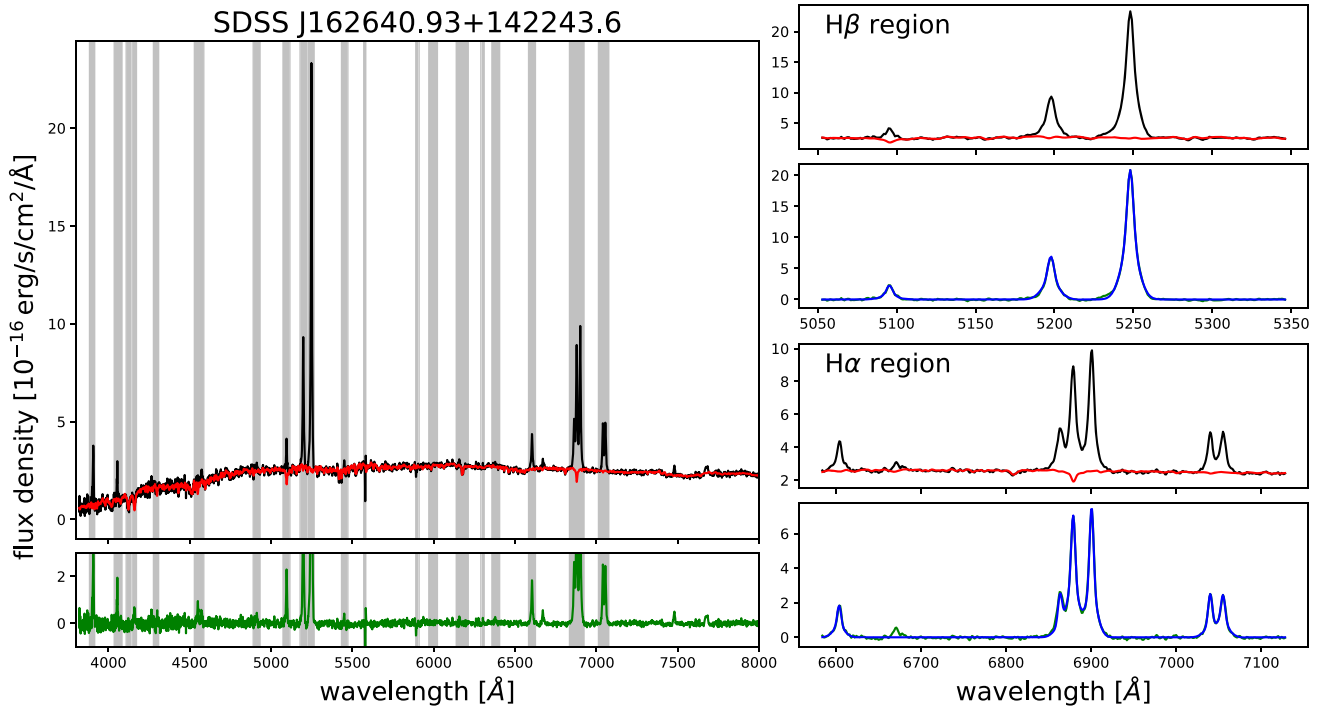


Figure A4. Same as Fig. 3 for SDSS J162640.93+142243.6.

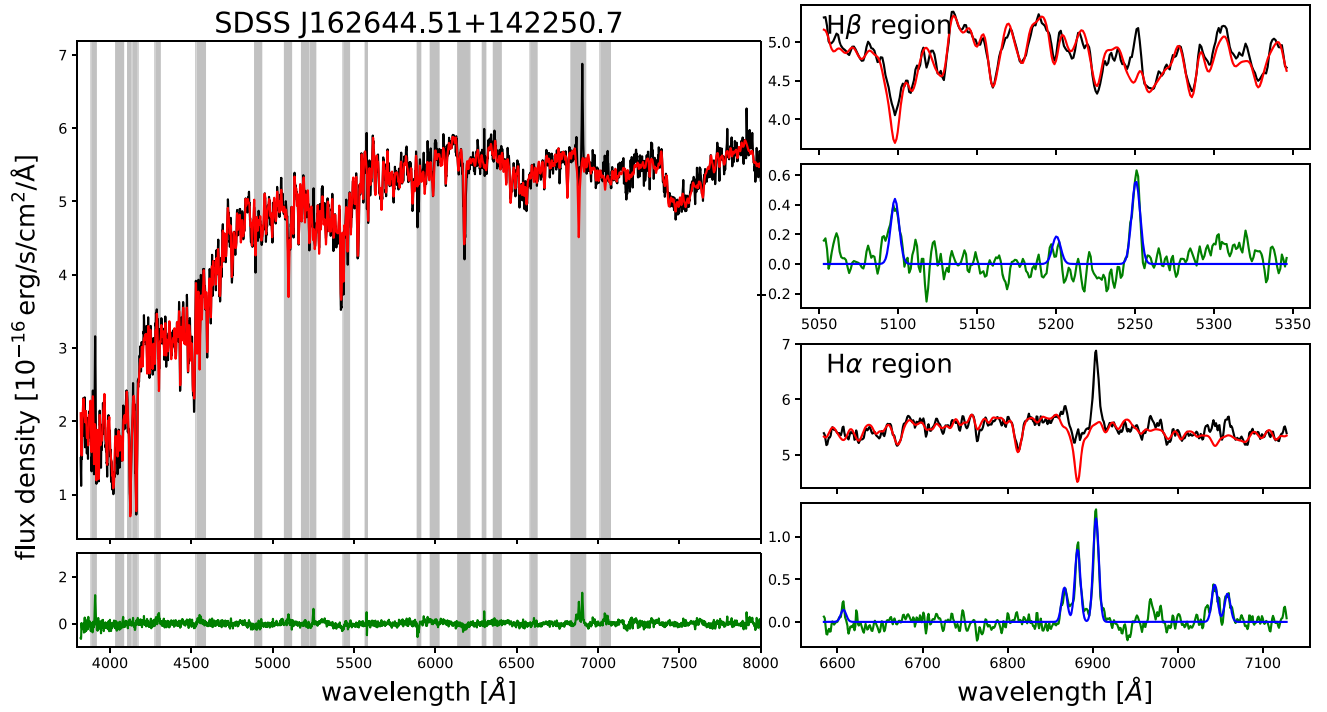


Figure A5. Same as Fig. 3 for SDSS J162644.51+142250.7.

This paper has been typeset from a $\text{\TeX}/\text{\LaTeX}$ file prepared by the author.